THESIS FOR THE DEGREE OF DOCTOR OF PHILOSOPHY
IN
THERMO AND FLUID DYNAMICS

A Study of Turbulent Natural Convection Boundary Layers Using Large-Eddy Simulation

DARIOUSH G. BARHAGHI

Department of Applied Mechanics

CHALMERS UNIVERSITY OF TECHNOLOGY

Göteborg, Sweden, 2007

A Study of Turbulent Natural Convection Boundary Layers Using Large-Eddy Simulation

DARIOUSH G. BARHAGHI
ISBN 978-91-7291-888-7

Doktorsavhandling vid Chalmers tekniska högskola
Ny serie nr 2569
ISSN 0346-718X

Division of Fluid Dynamics
Department of Applied Mechanics
Chalmers University of Technology
SE-412 96 Göteborg, Sweden

Tel.: +46-(0)31-7721000
Fax: +46-(0)31-180976

Printed at Chalmers Reproservice
Göteborg, Sweden 2007

To my parents, ***Nahid*** and ***Mostafa***

and

my wife, ***Parisa***

A Study of Turbulent Natural Convection Boundary Layers Using Large-Eddy Simulation

DARIOUSH G. BARHAGHI

Division of Fluid Dynamics
Department of Applied Mechanics
Chalmers University of Technology

Abstract

The structure of turbulent natural convection boundary layers in different geometries and the effect of the buoyancy on a mixed convection boundary layer are investigated. These geometries comprise a vertical finite cylinder, a vertical infinite channel, a cavity and a vertical finite channel.

In the three cases of vertical cylinder, cavity and finite channel, the boundary layer is in the state of development whereas in the case of the infinite channel, the boundary layer has a fully developed condition. In the vertical cylinder the natural convection is the dominant phenomenon although a small air-flow enters the geometry to reduce flow recirculations. In the cases of the vertical infinite channel and cavity there exists only a pure natural convection boundary layer. In the vertical finite channel, however, the boundary layer is of mixed convection type and radiation heat transfer affects its development owing to high channel wall temperatures.

The Grashof numbers based on the cylinder height, channel width, cavity and finite channel widths are $Gr = 5 \cdot 10^{11}$, $Gr = 9.6 \cdot 10^{5}$, $Gr = 3.9 \cdot 10^{8}$ and $Gr = 9.4 \cdot 10^{7}$, respectively.

The boundary layers are studied using two powerful numerical methods namely *Direct Numerical Simulation* or *DNS* and *Large Eddy Simulation* or *LES*. DNS is only used in the case of the vertical infinite channel. Three different sub-grid scale models are used in the case of the cavity and it is shown that the dynamic SGS model is the only model that is capable of predicting the location of the transition from laminar to turbulent flow correctly.

Mean flow parameters as well as turbulence parameters in all cases are studied and the results are compared with the existing experimental results. Comparisons are also made between the results of the vertical cylinder and experimental results obtained from a vertical flat plate.

Keywords: *LES*, *DNS*, natural convection boundary layer, free convection, vertical cylinder, cavity, radiation heat transfer

List of Publication

This thesis is based on the work contained in the following papers:

I Barhaghi, D. G., Davidson, L. & Karlsson, R. 2003 Natural convection heat transfer in a vertical shell and tube. Report 03/01. Dept. of Thermo and Fluid Dynamics, Chalmers University of Technology, Göteborg, Sweden.

II Barhaghi, D. G., Davidson, L. & Karlsson, R. 2006 Large-eddy simulation of natural convection boundary layer on a vertical cylinder. *International Journal of Heat and Fluid Flow* 27(5), 811-820.

III Barhaghi, D. G. & Davidson, L. 2006 Natural Convection Boundary Layer in a 5:1 Cavity (submitted for publication). *Physics of Fluids*.

IV Barhaghi, D. G. & Davidson, L. 2006 LES of mixed convection boundary layer under influence of radiation. Report 06/04. Dept. of Applied Mechanics, Chalmers University of Technology, Göteborg, Sweden.

V Barhaghi, D. G. & Davidson, L. 2007 On the validity of the Boussinesq approximation in a developing mixed convection boundary layer. *Thermal Issues in Emerging Technologies, Jan 3-6*, Cairo, Egypt.

VI Barhaghi, D. G. & Davidson, L. 2007 A comparison between natural convection boundary layers in different geometries. Report 07/01. Dept. of Applied Mechanics, Chalmers University of Technology, Göteborg, Sweden.

Other Relevant Publications

Barhaghi, D. G. 2004 DNS and LES of turbulent natural convection boundary layer. Thesis for Licentiate of Engineering 04/05. Dept. of Thermo and Fluid Dynamics, Chalmers University of Technology, Göteborg, Sweden.

Barhaghi, D. G. & Davidson, L. 2006 LES of mixed convection boundary layer between radiating parallel plates. In *Turbulence, Heat and Mass Transfer5* (ed. K. Hanjalić, Y. Nagano & S. Jakirlić), CD-ROM. New York: begell house, inc.

Acknowledgments

This work was conducted at the Division of Fluid Dynamics at Chalmers University of Technology.

I would like to express my sincere gratitudes to Professor Dr. Lars Davidson for his support and guidance throughout the course of this work. This thesis would never reach to this point without his enlightening discussions and brilliant advice.

I would like to thank Professor Dr. Rolf I. Karlsson and Dr. Shia-Hui Peng for sharing their ideas and knowledge.

I also would like to thank Monika Orrbacke, Sandra Arvidson and Ulla Lindberg-Thieme for their administrative support.

I am grateful to all of my colleagues especially Niklas Andersson, Mattias Billson and Andreas Sveningsson for taking their time to fix my computer-related problems and Magnus Stridh for the wonderful time that we have had together.

Financial support from the Swedish Research Council and the computer resources which have been provided by the Center for Parallel Computing (PDC), KTH are greatly acknowledged.

My warmest and deepest sense of gratitude goes to my family especially my parents, my wife, Parisa, and my family in Sweden for their unconditional support and understanding.

Nomenclature

$C_{\varepsilon 1}, C_{\varepsilon 2}$	turbulence model constants
C_k, C_μ	turbulence model constants
$C_\omega, C_{\omega 1}, C_{\omega 2}$	turbulence model constants
c_p	fluid specific heat at constant pressure
$\hat{e}_x$	unit vector in x-direction
$\hat{e}_y$	unit vector in y-direction
$\hat{e}_z$	unit vector in z-direction
$f_\varepsilon, f_k, f_\mu$	turbulence model damping functions
g_i	gravitational acceleration in i-direction
H	height of the vertical cylinder and cavity
h	convection heat transfer coefficient
k	turbulence kinetic energy; fluid thermal conductivity
P_k	turbulence production
Pr_t	turbulent Prandtl number, 0.9 for RANS models and 0.4 for LES
P	pressure
P^*	modified pressure (gravitational force subtracted)
q_w	wall heat flux, $-k(\partial T/\partial y)_{y=0}$
R_i	hot tube (inner cylinder) radius
R_o	shell (outer cylinder) radius
t	time
t^*	friction temperature, $q_w/(\rho c_p u^*)$
T	mean (time averaged) temperature
$\overline{T}$	filtered temperature
T_c	cold wall temperature, the ambient temperature or the inlet temperature
T_f	film temperature, $(T_h[K] + T_c[K])/2$
T_h	hot wall temperature
T_{ref}	reference temperature
T^+	dimensionless temperature, $(T_w - T)/t^*$
u	velocity component in x-direction

u_{max}	maximum velocity in the boundary layer
u^*	friction velocity parallel to the wall, $\sqrt{\tau_w/\rho}$
u^+	dimensionless velocity, U/u^*
$\overline{u}$	filtered velocity component in x-direction
$\overline{u}_i$	filtered velocity component in i-direction
U_i	mean (time averaged) velocity in i-direction
U_o	buoyant velocity, $\sqrt{g\beta(T_h - T_c)H}$
U_{bulk}	bulk velocity
v	velocity component in y-direction
$\overline{v}$	filtered velocity component in y-direction
$\mathbf{V}$	velocity vector, $u\hat{e}_x + v\hat{e}_y + w\hat{e}_z$
$\Delta\mathcal{V}$	cell volume
w	velocity component in z-direction
$\overline{w}$	filtered velocity component in z-direction
W	width of the cavity and distance between the inner and outer cylinder, $R_o - R_i$
x	stream-wise direction
Δx^+	dimensionless stream-wise cell length, $u^*\Delta x/\nu$
y	wall normal or radial direction
y_n	normal distance from the wall
y^+	dimensionless distance from wall, $u^* y_n/\nu$
y_{max}	location of maximum velocity with respect to the wall
Δy	cell width in wall normal direction
Δy^+	dimensionless wall normal cell length, $u^*\Delta y/\nu$
z	span-wise or angular direction
Δz	cell length in span-wise or angular direction
Δz^+	dimensionless span-wise cell length, $u^*\Delta z/\nu$; $u^* y\Delta\theta/\nu$

Greek Symbols

α	thermal diffusivity, $k/(\rho c_p)$
β	coefficient of expansion, $1/T_f[K]$
δ	half of the width of the infinite vertical channel
η	Kolmogorov length scale
ε	turbulence dissipation rate
Γ	thermal diffusion coefficient
κ	wave number
μ	fluid dynamic viscosity

ν_{eff}	effective kinematic viscosity
ν_t	turbulent kinematic viscosity
ω	specific dissipation, $\varepsilon/(0.09k)$
ρ	fluid density
$\sigma_\varepsilon, \sigma_k, \sigma_\omega$	turbulence Prandtl numbers
τ_w	wall shear stress, $(\mu \partial U/\partial y)_{y=0}$
θ	azimuthal angle and span-wise direction in cylindrical coordinate system
$\Delta\theta$	cell width in radian in cylinderical coordinate system
θ_t	dimensionless temperature, $(T - T_{ref})/(T_w - T_{ref})$
ζ	dimensionless transverse coordinate, $-y(\partial\theta_t/\partial y)_{y=0}$

Dimensionless quantities

C_f	friction coefficient, $\tau_w/(\rho U_o^2/2)$
Gr	local Grashof number, $g\beta(T_w - T_{ref})x^3/\nu^2$
Nu	local Nusselt number, $-x(\partial T/\partial y)_w/(T_h - T_c)$
Pr	Prandtl number, ν/α
Ra	local Rayleigh number, $g\beta(T_w - T_{ref})x^3/(\nu\alpha)$
Ri	local Richardson number, the ratio of potential to kinetic energy, gx/u^2

Subscript

c	cold
h	hot
w	wall
ref	reference

Contents

Chapter 1

Introduction

1.1 Heat Transfer

The importance of the heat transfer phenomenon continues to make it a major field of interest to engineers, designers and manufacturers. As this phenomenon exists in every aspect of life, a better understanding of it can lead to benefits for mankind. The applications include not only industrial aspects like power generators, reactors, turbines, heat exchangers and other power conversion devices, but also natural aspects like atmospheric and oceanic currents, bio-heat transfer, green house effects and heat transfer in stellar atmospheres.

A consideration of the number of conferences which take place each year and published books, journals, articles and papers as well as awards which are bestowed to scientist who have had an important contribution to development of this science, reveals the importance of this subject. According to Goldstein *et al.* (2002) there have been at least 18 conferences and 24 published books about related aspects of heat transfer and its applications in year 2000.

Heat transfer takes place in three forms: *Conduction, Convection and Radiation.* The major concern of this study is the *Natural Convection Heat Transfer* and *Numerical methods* are used as the analysis tools.

1.2 Natural Convection

Convective heat transfer is divided into three fields, namely *Forced Convection*, *Natural* or *Free Convection* and the combination of both, i.e. *mixed convection*. Forced convection heat transfer, is a process in which the heat transfer among different phases or states, occurs because of the velocity and temperature differences among them. It has primarily the characteristics of a molecular diffusion process which has been enhanced because of mixing process that is generated by momentum differences. On the other hand, natural convection heat transfer takes place because of density differences in a liquid or gas phase. The density difference which is mostly caused by the temperature difference, along with the gravitational force, creates a so called buoyancy force which consequently creates a momentum difference. However, it should be mentioned that not every temperature gradient causes movement in the fluid. In fact, temperature difference should be in a way that provokes instability in the fluid. It is conventional to use *unstable* temperature difference to emphasize this difference. This is shown in Figure 1.1.

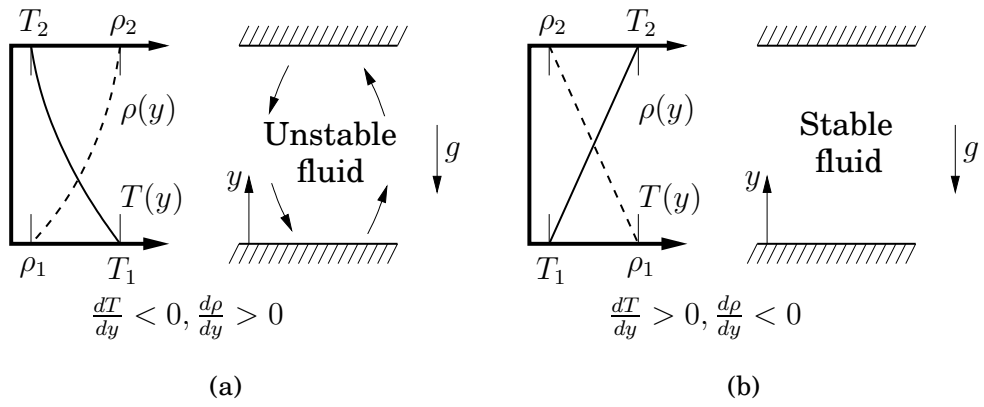

Figure 1.1: Unstable and stable fluid between two differentially heated horizontal walls.

Basically any forced convection heat transfer process comprises natural convection heat transfer since temperature difference results in density difference. However due to small contribution compared to forced convection counterpart, natural convection is sometimes neglected.

Usually, Nusselt number is considered in the form of $Nu_L = f(Re_L, Gr_L, Pr)$, where L is a characteristic length. When the inequality $(Gr_L/Re_L^2) \ll$

1 holds, free convection effects may be neglected. Conversely, when $(Gr_L/Re_L^2) \gg 1$, forced convection effects may be neglected and in case of $(Gr_L/Re_L^2) \approx 1$ a combined effect of free and forced convection must be considered.

The number of heat transfer applications in which the natural convection is a dominant phenomenon is large and better understanding of this phenomenon has even increased the number of applications and has led to a number of sophisticated industrial and environmental designs. Whenever running costs are important or small efficiency improvements are vital and can play a vital role in energy consumption, this type of heat transfer is bound to come under scrutiny. Oceanographic and atmospheric problems such as green house effects, Gulf stream and extreme climate changes, design of electrical and electronic devices, home appliances such as refrigerators, cooling towers, safety of reactors, economic conversion of saline to fresh water and direct contact exchangers are all problems that have given a particular concern to this science.

1.3 Previous Investigations

Natural convection heat transfer has been extensively studied experimentally as well as numerically and analytically during past decades. Many experiments on the laminar natural convection heat transfer boundary layer have been performed and the results are shown by Burmeister (1993). These experiments have been conducted for various ranges of Prandtl numbers and many useful correlations between Nusselt and Rayleigh numbers are proposed.

Similarity solutions for the laminar natural convection heat transfer boundary layers at different Prandtl numbers which were carried out by Ostrach (1952), yielded results that were in good agreement with experiments.

Turbulent natural convection boundary layer next to a heated vertical surface was analysed by George & Capp (1979). In this theoretical investigation, the boundary layer is treated in two parts. An inner region in which the mean convection terms are negligible and is identified as constant heat flux layer and an outer region in which conduction terms are considered negligible. The inner region is shown to be very narrow whereas the outer region constructs most of the boundary layer. In

this work, universal velocity and temperature profiles for asymptotic values of Rayleigh number when approaches infinity are suggested for both constant heat flux and constant temperature boundary conditions. The proposed theory was modified later by Wosnik & George (1995) and it was claimed that the new scaling functions were valid both in the limit of infinite Rayleigh number and for any position downstream well into the turbulent regime. It was also shown that the boundary layer showed no linear growth for moderate Rayleigh numbers but asymptotically lost its stream-wise inhomogeneity where it grows linearly.

Experiments of the turbulent natural convection heat transfer boundary layer in air were conducted by Warner & Arpaci (1968) and Cheesewright (1968). Some experiments were also carried out in different liquids by Lock & Trotter (1968), Vliet & Liu (1969), Fujii *et al.* (1970) and Kutateladze *et al.* (1972). In all of these experiments, the overall characteristics of the natural convection were studied.

Cheesewright *et al.* (1986) studied the natural convection boundary layer in a rectangular cavity filled with air and having an aspect ratio of five. Since it was in practice difficult to establish a perfectly insulated boundary in the experiment, an asymmetric flow was reported. The reason was principally the imperfect insulation at the ceiling of the cavity where the heat loss, although very small, prohibits the flow from relaminarization. However, relaminarization at the floor of the cavity does take place.

Turbulent transport in a natural convection boundary layer along a vertical flat plate was experimentally studied by Kitamura *et al.* (1985) and it was shown that the large eddy motions play an important role for the turbulent transport. Later, Tsuji & Nagano (1988*a*) performed an experimental study of natural convection heat transfer boundary layer in more details compared to previous studies. Characteristics of the near wall region was studied and applicability of the conventional analogy between heat and momentum transfer and the concept of the viscous sublayer for natural convection were investigated. The structure of turbulent natural convection boundary layer was studied further by Tsuji & Nagano (1988*b*) and it was shown that this flow has a unique turbulent structure which is rarely seen in other turbulent boundary layers. The results suggest that for values of y^+ between 20 to 100, $\overline{u'v'}$ is not correlated with the mean velocity gradient, i.e. $\partial U/\partial y$.

Turbulent natural convection around a heated vertical slender cylinder was studied by Persson & Karlsson (1996) and new turbulent structures were presented for the near wall region. It was shown that there

exists a region of negative shear stress close to the cylinder contrary to the measurements of Tsuji & Nagano (1988*b*).

Low turbulence natural convection in an air filled square cavity was studied and the results for the thermal and fluid flow fields and turbulence quantities were published by Tian & Karayiannis (2000*a*) and Tian & Karayiannis (2000*b*), respectively. The experiments were conducted at a relatively low Rayleigh number $Ra = 1.58 \cdot 10^9$ and the contour plot of the thermal field and a vector plot of air flow in the cavity were reported for the first time. It is believed that in this experiment, the level of turbulence has been quite low, and the flow has been only transitional with a stratified quiescent flow in the core.

Another experiment was conducted by Betts & Bokhari (2000) to study the flow and heat transfer in a cavity which was thin enough to make the flow in the core region fully turbulent. The experiment was performed at two different Rayleigh numbers, $Ra = 0.86 \cdot 10^6$ and $Ra = 1.43 \cdot 10^6$, based on the cavity width. The advantage of having a tall and thin cavity was that it made it easier to achieve two dimensional results.

The Natural convection boundary layer has also been studied numerically. Many *LES* and *DNS* investigations have been carried out and useful results are proposed.

LES of natural convection in concentric horizontal annuli was studied by Miki *et al.* (1993) and the results were compared with available experimental results. The maximum Rayleigh number based on the gap width was $1.18 \cdot 10^9$. It was shown that by ignoring SGS model in the governing equations, very different results for fluctuating quantities were achieved, although the results for overall flow quantities such as velocity and temperature remained reasonably intact. It was shown that the accumulation of energy in small scales caused this problem. Also it was shown that by increasing the Smagorinsky constant from 0.1 to 0.2, the ratio of SGS energy to grid scale energy increased drastically.

Peng & Davidson (1998) studied the effect of different SGS models and proposed a new SGS model for buoyancy affected turbulent flows. The three studied SGS models were a scalar model which has no term to take the effect of buoyancy into account, a buoyancy model which was proposed by Eidson (1985) and a modified model based on the buoyancy model. The motivation for proposing the modified model was the resulting non-real solutions in cases where the buoyancy term was

larger than the strain rate tensor. It was shown that all the models despite of very different coefficients gave similar results when applied to a Rayleigh-Bénard problem with a Rayleigh number equal to $3.8 \cdot 10^5$. Low influence of small scales on the large scales and low turbulence level of the considered Rayleigh-Bénard problem was mentioned to be the likely reasons for the similarity of results.

Ningyu *et al.* (2000) proposed a new dynamic SGS model for LES of stratified flows. The new model was then applied to a Rayleigh-Bénard problem at different Richardson numbers and it was shown that for Richardson numbers larger than a critical 0.06 value, the flow showed a laminar behavior. The obtained critical Richardson number was shown to be in good agreement with theoretical value of 0.0554.

Zhang & Chen (2000) proposed a new dynamic SGS model which is based on a new defined averaging method in order to calculate the dynamic SGS viscosity coefficient when no homogeneous direction in the computational geometry exists. The motivation for the proposed model was that due to high fluctuations of the SGS coefficient in dynamic models, convergence is highly unstable. The proposed model is claimed to be useful for indoor airflows in which there is generally no homogeneous direction involved. The performance of the model is investigated by comparing the results for three different cases of pure natural, forced and mixed convection in different cavities with the existing experimental results.

LES of a turbulent rotating convective flow was performed by Cui & Street (2001). In this study, the adopted geometry consisted of a circular tank of radius $R_o = 0.48m$ and the fluid was water. A heat exchanger of radius $R_i = 0.2m$ was set up below the tank. Results were obtained for different rotational speeds and heat fluxes. It was shown that neither the angular velocity nor heat flux affect the growth of the conductive layer which forms over the heating plate below the tank. It was also shown that the convective rings which form near the bottom of the tank, are increasingly uniform with increasing angular velocity. It is also shown that the time that it takes for the rings to reach the top of the tank is independent of the angular velocity. Furthermore it was shown that the number of convective rings depends on the heat flux.

Peng & Davidson (2001*b*) studied the LES of turbulent flow in a confined cavity and compared the results with the experiment of Tian & Karayiannis (2000*a*) and Tian & Karayiannis (2000*b*). It was shown that mean flow quantities were in good agreement with the experimental results, however, there were some discrepancies in the prediction of

turbulence statistics especially in the shear layer region between the wall boundary layer flow and the cavity core region. It is suggested that special attention should be paid to the flow physics and numerical treatment in this region. A comparative study of LES of turbulent buoyant flow in a cavity with different SGS models and grid resolutions was also performed by Peng & Davidson (2001*a*). It was shown that although the proposed SGS model was able to predict mean flow quantities, it was unable to recreate the turbulence quantities particularly in the core region. It was also shown that the energetic flow structures which are enhanced by buoyancy in the boundary layer along the heated and cooled walls of the cavity, exist in the outer layer neighboring the nearly stagnant core region of the cavity. Existence of a k^{-3} buoyancy subrange next to the $k^{-5/3}$ inertial subrange was confirmed by the results. It was suggested that a span-wise mesh spacing of $\Delta z^+ \approx 20$ is appropriate to resolve the energetic, coherent structures in the boundary layer. Peng & Davidson (2002) in continuation of previous works, proposed a new non-linear SGS heat-flux model. The model is to some extent similar to a scale-similarity model subjected to a Taylor expansion for the filtering operation. The model was examined in an infinite vertical channel with differentially heated walls and it was shown that very encouraging results compared to DNS and experimental results were achieved.

Natural convection boundary layers are also studied by DNS. As it is very hard to resolve the smallest scales, only simple geometries have been studied so far. Paolucci & Chenoweth (1987) studied cavities with different aspect ratios using direct numerical simulation (DNS). The simulations were performed using two-dimensional low Mach number model Navier-Stokes and temperature equations. They found that, for aspect ratios of approximately three or larger, the transition from steady state is caused by instability of the sidewall boundary layers whereas, for smaller aspect ratios, it is due to internal waves near the departing corners.

Two-dimensional turbulent natural convection in an enclosed square cavity was studied by Paolucci (1990) using DNS. The corresponding Rayleigh number based on the cavity width was 10^{10}. The transitional instabilities resulting in turbulence were studied and large scale structures were shown to exist. The structure of the turbulence was accurately explained and contrary to the results of Tsuji & Nagano (1988*a*) and Tsuji & Nagano (1988*b*), a negative region for the shear stress in the vicinity of the wall could be observed in the results.

Using DNS, natural convection between two vertical differentially heated walls was studied by Nieuwstadt & Versteegh (1997). The major topic of investigation in this study was the self similarity behavior of the results following the scaling hypothesis proposed by George & Capp (1979). It was shown that the proposed scaling approach leads to self-similarity for the mean temperature profile but it fails for the mean velocity profile. The adopted geometry dimensions in this study was $7.6\pi\delta \cdot 4\pi\delta \cdot 2\delta$ in stream-wise, span-wise and cross stream-wise directions, respectively. In another study, Versteegh & Nieuwstadt (1998) investigated the turbulent budgets of natural convection in an infinite, differentially heated, vertical channel. It was found that close to the wall, the shear production of turbulence was negative.

DNS of a plane vertical channel flow, in order to study the difference between the case with buoyancy and the case without buoyancy was performed by Davidson *et al.* (2003). It was found that in the case without buoyancy or forced convection case, the turbulent shear stress balances the pressure gradient in the region away from the viscous dominated region. However, in the case with buoyancy or mixed convection case, it is shown that the buoyancy term modifies the shear stress in a way that the shear stress is decreased near the hot wall where the flow is aided by buoyancy and increased near the cold wall where the flow is opposed by buoyancy. This is shown to be the case for all normal stresses as well. However, it is shown that $\overline{t'^2}$ behaves in a different way compared to the Reynolds stresses. It increases near the hot wall and decreases near the cold wall.

Soria *et al.* (2004) studied the effect of three dimensionality on the first and the second order statistics for a cavity with an aspect ratio of four using direct numerical simulation. The flow in this case was weakly turbulent and it was shown that the results of the two-dimensional computations were in good agreement with the results of the three-dimensional computations in the case of first order statistics. However, the Reynolds stresses and turbulent heat fluxes deviated considerably from each other, especially near the top and the bottom of the cavity.

These extensive researches seem to be continuing in the future until the structure of this type of boundary layer is fully understood and the developed experimental and numerical tools result in a general consensus among the scientists. In this regard, this work aims to study the natural convection boundary layer in different geometries to investigate the differences and similarities that exist between them.

1.4 Overview of the Present Study

This work is divided into three major parts. In Chapter 2, the geometry configurations that have been adopted in this study are shown and explained.

In Chapter 3, the numerical methods that have been used are explained. These methods consist of *RANS*, *LES* and *DNS*. In the case of the *RANS* computations the $k-\omega$ model is used. In the case of the *LES* computations different *SGS* models are used and *DNS* computations are basically the *LES* computations on a fine enough mesh for which *SGS* models are dropped.

In Chapter 4, the results are presented briefly and compared with the existing experimental results. Chapters 5 makes some concluding remarks and in Chapter 6 suggestion are made for the future work.

Chapter 2

Geometrical Configurations

Geometries that are used in this study are mainly adopted from experimental setup configurations. These geometrical configurations are made as simple as possible since the aim of the study is the boundary layers' structures and formations. Although the geometries are simple, the flow and heat transfer structures are still so complicated by themselves which is another reason why these configurations are made simple.

As *LES* computations are time consuming these geometries are furthermore simplified so that time-averaged two dimensional results can be obtained. The geometries, their dimensions and the boundary conditions are listed and explained as follows.

2.1 Vertical Cylinder

In contrast to the natural convection boundary layer on vertical flat plates for which many investigations are made and results exist in the literature, few experiments and simulations are made to study this boundary layer on a vertical slender cylinder. This fact and existence of an experimental apparatus in the laboratory of the Department, created the motivation for designing an *LES* problem in order to study the natural convection heat transfer along a vertical cylinder. The schematic diagram of the experimental apparatus is shown in Figure 2.1.

Water temperature is kept at 80^oC and is circulated in counter flow

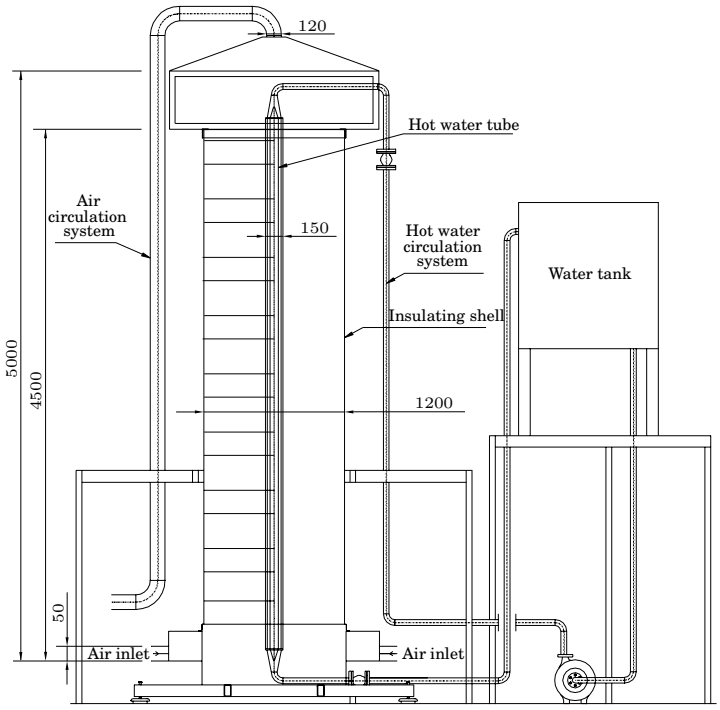

Figure 2.1: Experimental apparatus.

with respect to the air flow surrounding it. The incoming air is kept at 25^oC with an HVAC unit which is not shown in the figure. Both at the inlet and near the outlet at the height of $4.5m$ perforated plates are used in order to make the flow at the inlet and outlet smooth and uniform. The maximum local Grashof number reaches approximately $Gr = 5 \cdot 10^{11}$ in this apparatus. The reason for constructing a bigger cylinder as a shell to enclose the inner hot cylinder is that although an idealized vertical natural convection boundary layer takes place in infinite surroundings, it is impossible to achieve such an ideal condition either in experiments or in numerical calculations. In fact, both experiments and calculations are very sensitive to the location of the infinite boundaries and any disturbances there (Persson & Karlsson, 1996). Another advantage of this geometrical configuration is that it makes it possible to create a truly two dimensional time-averaged fluid flow and heat transfer.

The HVAC unit supplies air at low speed into the inlet which is located near the bottom of the isolating shell. The reason for blowing the air is to prevent the temperature stratification along the boundary layer. This is shown in Figure 2.2 in two dimensional format.

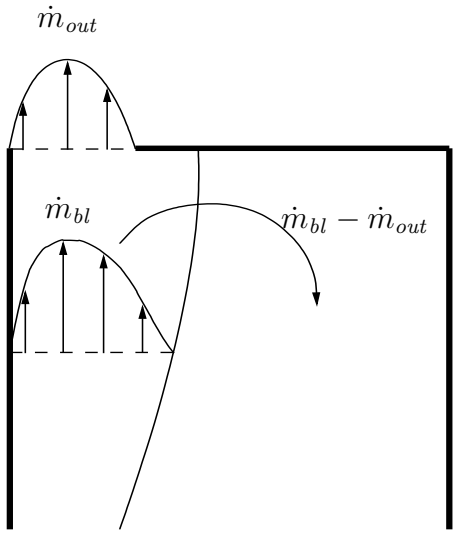

Figure 2.2: Temperature stratification due to recirculation.

If the rate of the fluid flow inside the boundary layer approaching the outlet ($\dot{m}_{bl}$) becomes larger than the inlet flow rate ($\dot{m}_{in} = \dot{m}_{out}$), some part of the fluid ($\dot{m}_{bl} - \dot{m}_{in}$) will recirculate in order to compensate for this difference. The recirculating fluid increases the fluid temperature in the outer part of the boundary layer. This leads to temperature stratification alongside the boundary layer causing the boundary layer growth to be affected owing to the decreased buoyancy force. However, by increasing the inlet flow rate, a smaller flow recirculation and consequently a smaller temperature stratification is likely to occur.

Since the existence of the perforated plates would make the *LES* computations more difficult and time consuming, further geometry simplifications were necessary. The process of geometry simplification was made through 2D-*RANS* simulations. This is shown in Figure 2.3 (for details refer to Barhaghi *et al.* (2003)).

Through these simulations the operating condition of the experimental rig is also designed. Based on these preliminary studies, the three-dimensional geometry which is used for *LES* computations is shown in Figure 2.4.

2.1.1 Boundary Conditions

From the *RANS* computations, the inlet velocity is set to $U_{in} = 0.6m/s$. The temperatures at the inlet and on the hot inner cylinder are adopted

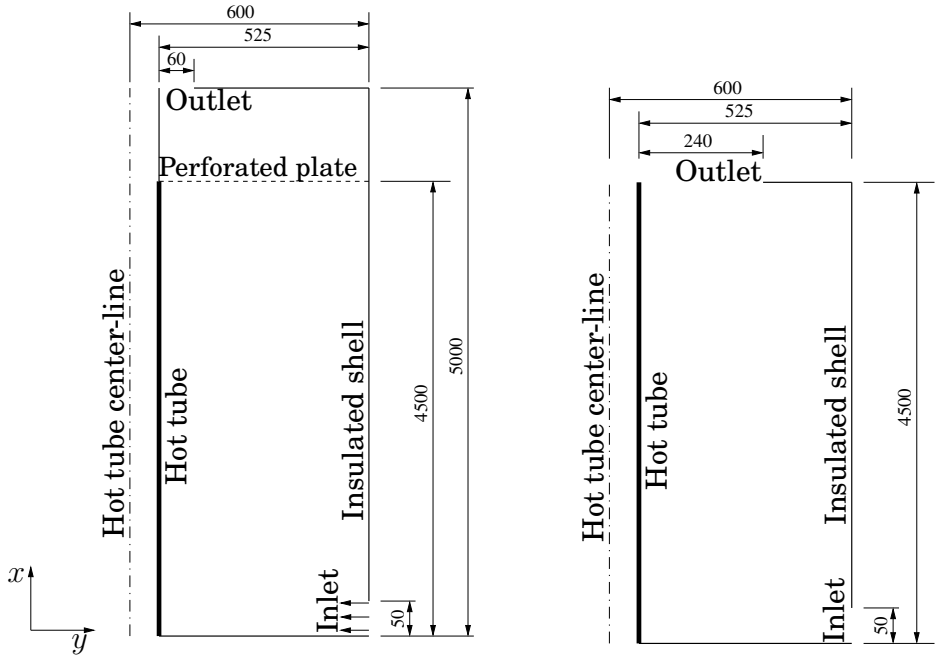

(a) 2D Computational geometry.

(b) Simplified Geometry.

Figure 2.3: Geometry simplification using 2D *RANS* simulations. Dimensions are in millimeters and figures are not to scale.

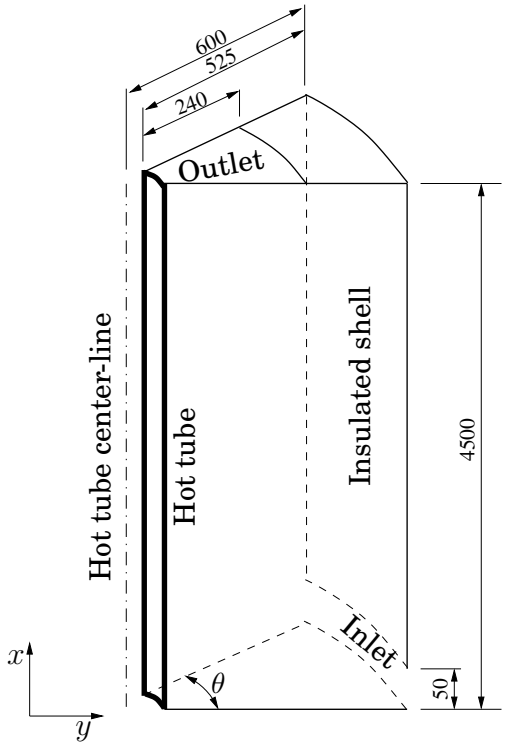

Figure 2.4: *LES* Computational geometry.

from the operating condition of the experimental apparatus, i.e. $T_{in} = 25^oC$ and $T_h = 80^oC$, respectively. At the outlet, for the temperature and velocities, a convective boundary condition (Sohankar *et al.*, 1998) is applied:

$$\frac{\partial \phi}{\partial t} + U_{bulk} \left(\frac{\partial \phi}{\partial x} \right)_{outlet} = 0 \tag{2.1}$$

Here, ϕ stands for the velocities and temperature and x is the perpendicular direction to the outlet surface. The outer cylinder in the experimental apparatus is made of fibreglass which makes it a good insulation. Therefore adiabatic boundary condition is applied to the outer cylinder and other surfaces except the hot cylinder.

In the span-wise (angular) direction (θ) periodic boundary condition is applied assuming that the turbulence is homogeneous in this direction. The problem in this case is the width of the computational domain in the angular direction. The domain should be wide enough to capture the largest eddies of the flow. This ensures that the energy of turbulence is captured correctly in the simulation which is an important issue to yield correct magnitude of turbulence parameters.

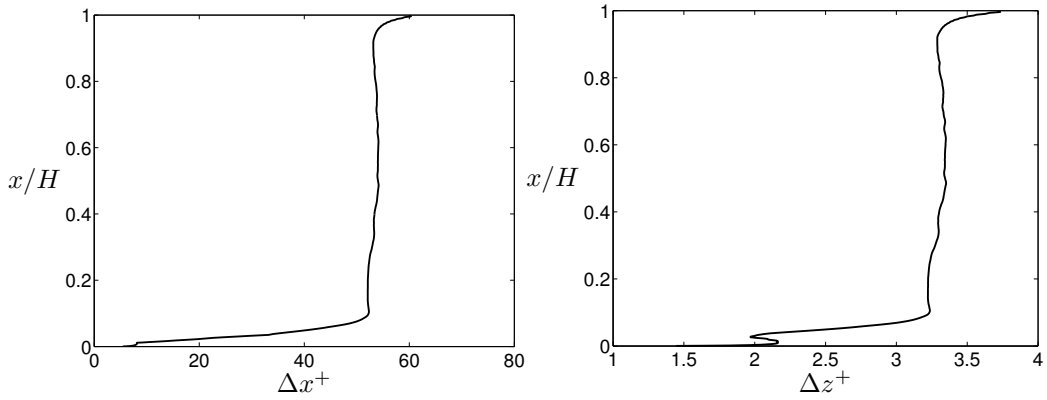

(a) Stream-wise cell sizes.

(b) Span-wise cell sizes.

Figure 2.5: Near wall spacing of the mesh in viscous units.

In this study several computational domains with angular widths of $\theta = 18^o,\ 36^o, \ldots,\ 126^o,\ 162^o$ are used to find the required angle for obtaining domain independent results. A comparison between the results of the two last angles shows that the results are almost independent of the computational domains at these angles.

2.1.2 Grid Specifications

In this study it is tried to fulfil the criteria which are in accordance with the conventional grid resolutions in *LES* computations that is $y^+ \leq 1$, $\Delta x^+ \leq 50$ and $\Delta z^+ \leq 25$ in the wall normal, the stream-wise and the span-wise directions, respectively, see e.g. Kaltenbach *et al.* (1999). However in most of the cases more restricted criteria are used since the natural convection boundary layers are inherently different from the forced convection boundary layers.

In this case, a 3% mesh stretching is used near the wall and far from it a 9% stretch is applied. The number of nodes in the case of $\theta = 18^o$ is $402 \times 98 \times 34$ in the stream-wise (x), wall normal or radial (y) and span-wise or angular (z) directions, respectively. The respective number of nodes in the case of $\theta = 162^o$ is $402 \times 98 \times 290$.

The resulting mesh sizes in viscous units in the stream-wise and span-wise directions are shown in Figures 2.5(a) and 2.5(b).

As can be seen, in the stream-wise and span-wise directions $\Delta x^+ \leq 50$

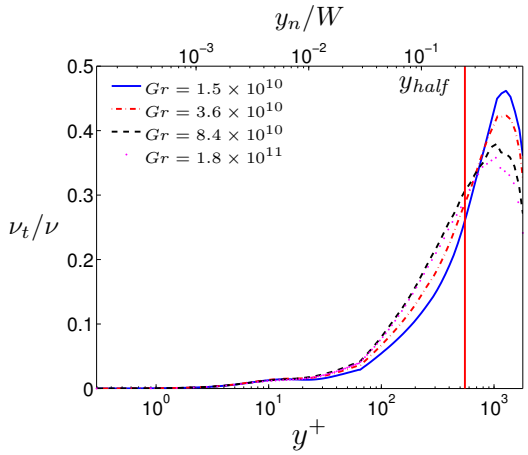

Figure 2.6: *SGS* viscosity variation across the boundary layer at different heights.

and $\Delta z^+ \leq 3.5$ in the major part of the computational domain, respectively. In other words all the cells which lie in $y_n \leq (R_o - R_i)/2$ have a $\Delta z^+ \leq 15$.

Finally, as Smagorinsky *SGS* viscosity depends on grid size, its magnitude can give an insight into how fine the mesh is. Figure 2.6 shows the turbulent viscosity normalized by the viscosity at different heights. The vertical line shows the boundary layer thickness (y_{half}) which is defined to be the location at which the velocity is half of the maximum boundary layer velocity. It can be seen that the *SGS* viscosity is, at maximum, less than half of the laminar viscosity and it occurs far from the wall. In fact in the major part of the boundary layer, this ratio remains less than 0.3.

2.2 Infinite Vertical Channel

Fluid flow and heat transfer in an infinite vertical channel is an interesting flow configuration since both the velocity and temperature boundary layers are fully developed and the time averaged flow is one dimensional. Although the geometry is simple in this case the flow and turbulence structures are complicated. This configuration has always been a suitable test case for *RANS* models, although those models are incapable of capturing the turbulence correctly. One radical example is the turbulent heat transfer in the stream-wise direction ($\overline{u't'}$) which is under-predicted by *RANS* eddy-viscosity models.

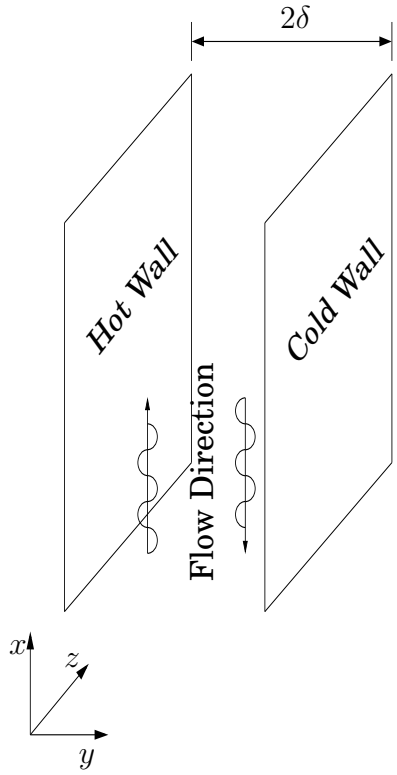

Figure 2.7: Channel flow geometry (not to scale).

DNS of fully developed natural convection in a vertical channel has been studied by Versteegh & Nieuwstadt (1998) and Davidson *et al.* (2003). From these investigations, it was believed that the results are very much dependent on the computational domain particularly the height of the solution domain. To investigate this, the *DNS* of the natural convection boundary layers in a vertical channel with differentially heated walls for three different domain heights have been studied and the results are compared. The computational domain is shown in Figure 2.7.

The three different domains which have been used for numerical calculations have dimensions of $7.6\pi \times 2 \times 2\pi$, $12\pi \times 2 \times 2\pi$ and $18\pi \times 2 \times 2\pi$ in the x, y and z directions, respectively.

2.2.1 Boundary Conditions

In this case, the continuity, Navier-Stokes and temperature equations are transformed into non-dimensional form and the following values

are used in the governing equations:

$$\begin{cases} Re = u_o h/\nu = 150 \\ T_h = 1,\ T_c = 0 \\ Pr = 0.7 \\ \delta = 1 \\ Gr = g\beta\Delta T(2\delta)^3/\nu^2 = 9.6 \times 10^5 \end{cases} \tag{2.2}$$

In Equation 2.2, ν is the kinematic viscosity, Pr is the Prandtl number, δ is half of the channel width, Gr is Grashof number based on the channel width and T_h and T_c are hot and cold channel wall temperatures, respectively.

To solve these equations, periodic boundary condition is applied in the stream-wise (x) and span-wise (z) directions and no-slip boundary condition is applied at the walls.

2.2.2 Grid Specifications

In all three cases, the same number of nodes is used in the wall-normal (y) and the span-wise (z) directions, that is 66×66 and a 7-percent stretch along the y axis is used. In the stream-wise direction, 82, 130 and 194 nodes are used for the lengths of $L = 7.6\pi$, 12π and 18π, respectively.

The resulting grid sizes in viscous units are approximately $\Delta x^+ = 20$ and $\Delta z^+ = 6.5$ in the stream-wise and the span-wise directions, respectively. The distance of the wall adjacent node from the wall is $y^+ < 1$ in all the cases.

2.3 Cavity

Cavity configurations have also been extensively studied in the literature. In this case a cavity with the aspect ratio of $AR = 5$ is studied using *LES* and different *SGS* viscosities. The boundary layer in this case includes regions of laminar, transitional and turbulent flow. Therefore, from a numerical point of view, it is a demanding task to capture the transition. Another problem from an experimental point of view is that this flow is extremely sensitive to the boundary conditions.

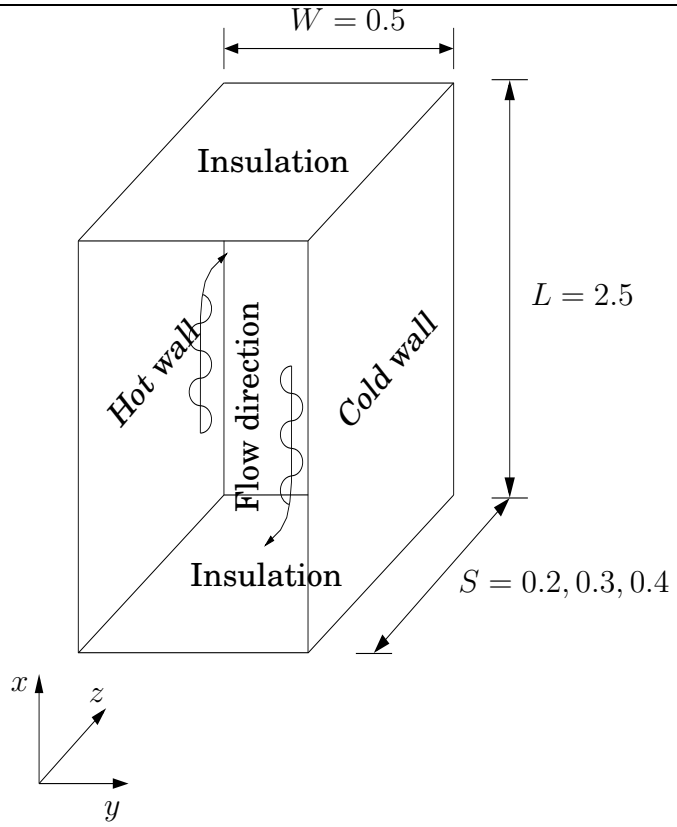

Figure 2.8: Cavity configuration with aspect ratio of $AR = L/W = 5$. All dimensions are in meters. Figure is not to scale.

The adopted geometry which resembles the experimental cavity configuration of Cheesewright *et al.* (1986) is shown in Figure 2.8. As can be seen, simulations are carried out for three different span-wise lengths to make sure that the energy of turbulence is appropriately captured via largest eddies.

2.3.1 Boundary Conditions

In this study, air is the working fluid in the cavity. The hot wall and the cold wall temperatures regarding Figure 2.8 are $T_h = 68^oC$ and $T_c = 22.2^oC$, respectively. Fluid properties are considered to be constant and are acquired for the air at the film temperature $T_f = (T_h + T_c)/2 = 45.1^oC$. The upper and the lower walls (horizontal walls) are assumed to be insulated and the adiabatic boundary condition is applied to the temperature at these walls. Consequently the Rayleigh number based on the width of the cavity is $Ra_W = g\beta(T_h - T_c)W^3/\nu\alpha = 4.028 \cdot 10^8$.

Similar to the previous geometries, periodic boundary condition is applied to all variables in the span-wise direction.

2.3.2 Grid Specifications

Two different grid resolutions with $162 \times 98 \times 42$ and $322 \times 98 \times 82$ nodes in the stream-wise (x), wall normal (y) and span-wise (z) directions, respectively, are used to carry out the simulations for the computational domain with $S = 0.2$. A stretch factor equal to 9% is applied to the grid in the wall normal direction in a way that the grid is kept symmetrical with respect to the middle of the cavity. Constant grid spacing is applied in the stream-wise (x) and span-wise (z) directions.

In the case of the fine grid, the acquired grid sizes in viscous units are $\Delta x^+ \leq 25$, $\Delta z^+ \leq 8$ and $y^+ \leq 0.6$. These values are obtained for the dynamic Smagorinsky *SGS* model.

2.4 Finite Channel

This case is an important and interesting case for which experiments are carried out by Wang *et al.* (2004). The experimental results in this case confirm the influence of the radiation heat transfer but they are only provided for one specific height.

The high temperature difference between the channel wall and the fluid makes this configuration a suitable case to investigate the validity of the Boussinesq approximation. Another interesting aspect of this case is the existence of the radiation that has many industrial applications.

The computational domain which is in accordance with the experimental rig is shown in Figure 2.9. The major difference between this domain and the experimental rig is that in the latter case, the length of the channel in the entrance region before the commencement of the wall heating is $1\ m$ compared to the former case which is $0.5\ m$. The length of the entrance region in the case of the computations is shortened to save some computational time and *CPU* work.

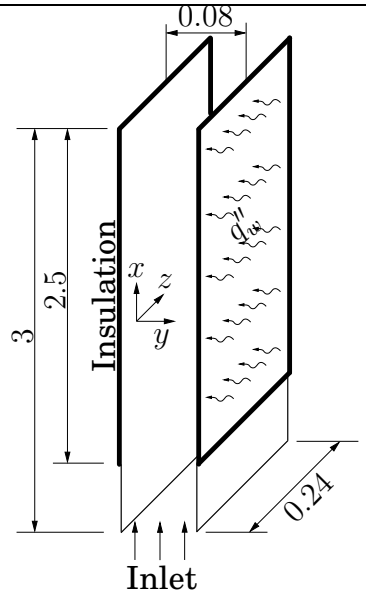

Figure 2.9: Finite channel geometry configuration. All the dimensions are in meters.

2.4.1 Boundary Conditions

The working fluid in this case is also air and regarding Figure 2.9, a constant heat flux $q''_w = 449\ W/m^2$ is applied to the hot wall at $x > 0.5\ m$ whereas the other wall is kept insulated. The Grashof number based on the wall heat flux and the channel width is $Gr_W = g\beta q''_w W^4/(\nu^2 k) \approx 9.4 \cdot 10^7$ in which $W = 0.08m$ and $\nu = 1.55 \times 10^{-5} m^2/s$. The air temperature at the inlet is $T_{in} = 18.6^o C$ and from initial *RANS* computations it was found that the temperature difference between the hot wall and the inlet reaches to as high as $100^o C$. This makes the radiation heat transfer from the hot wall to the insulated wall to be significant. Therefore the actual heat flux from the hot wall and the insulated wall are $q''_w - q''_{rad}$ and q''_{rad}, respectively. To calculate the radiation heat transfer, the emissivity of the channel walls is set to $\varepsilon = 0.125$ according to experiment.

At the inlet, the instantaneous *DNS* results of a fully developed channel are prescribed which yields a Reynolds number based on the bulk velocity and channel width equal to $Re_W = 5080$. Therefore the boundary layer is a mixed convection boundary layer for which the ratio of the Grashof number to the Reynolds number is $Gr_W/Re_W^2 \approx 3.6$. It can be concluded that in this boundary layer, the buoyancy effects are as important as the inertial effects.

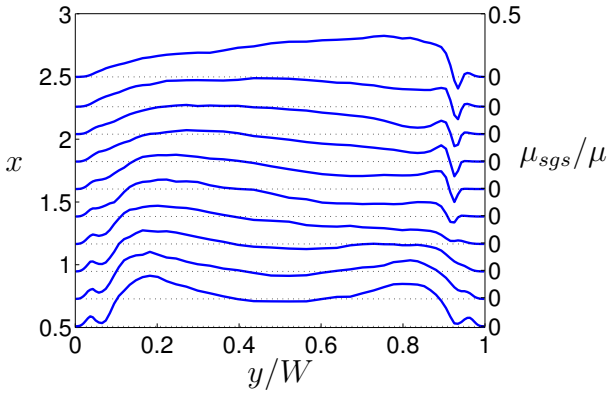

Figure 2.10: Profiles of $\langle \mu_{sgs} \rangle$ across the channel at different heights.

At the outlet, convective boundary condition has been applied to all variables:

$$\frac{\partial \phi}{\partial t} + \overline{u}^n \left(\frac{\partial \phi}{\partial x} \right)_{outlet} = 0 \tag{2.3}$$

Contrary to Equation 2.1, the advective velocity in this equation is time averaged from the first time step to the current time step and reads:

$$\overline{u}^n = \left[(n-1)\overline{u}^{n-1} + u^n \right] / n \tag{2.4}$$

in which n is the current time step and $n-1$ is the old time step.

2.4.2 Grid Specifications

In this case also two different grid resolutions with $322 \times 66 \times 50$ and $482 \times 66 \times 66$ number of nodes in the x, y and z directions, respectively, are used to carry out the computations. The obtained spatial resolutions in viscous units for the coarse grid, along the hot wall, are $\Delta z^+ < 45$ and $\Delta x^+ < 80$ in the span-wise and stream-wise directions. The respective values in the case of the fine grid are $\Delta z^+ < 33$ and $\Delta x^+ < 50$. In both cases $y^+ < 0.6$ for the wall adjacent node and 9% stretch factor is used in the wall-normal (y) direction.

The fine grid yields a turbulent viscosity which at maximum is about 40% of the fluid viscosity (see Figure 2.10).

Chapter 3

Numerical Methods

To solve the conservation of mass, momentum and energy equations, three different approaches are employed. These are *Reynolds Averaged Navier-Stokes* or *RANS*, *Large-Eddy Simulation* or *LES* and *Direct Numerical Simulation* or *DNS*. However, the main focus of this study is *LES*.

3.1 Mean Flow Equations

Mean flow equations are composed of conservation of mass, momentum and energy equations. These equations can be described in conservative form in Cartesian coordinate system.

3.1.1 Cartesian coordinate system

The set of conservation equations in conservative form and in Cartesian coordinate system reads:

Continuity:

$$\frac{\partial \rho}{\partial t} + \frac{\partial \rho \overline{u}_i}{\partial x_i} = 0 \tag{3.1}$$

Momentum equations:

$$\frac{\partial \rho \overline{u}_i}{\partial t} + \frac{\partial \rho \overline{u}_i \overline{u}_j}{\partial x_j} = -\frac{\partial \overline{P}}{\partial x_i} + \rho g_i + \frac{\partial}{\partial x_j}\left(\mu_{eff,v} \frac{\partial \overline{u}_i}{\partial x_j}\right) \tag{3.2}$$

Temperature equation:

$$\frac{\partial \rho \overline{T}}{\partial t} + \frac{\partial \rho \overline{u}_j \overline{T}}{\partial x_j} = \frac{\partial}{\partial x_j}\left[\Gamma_{eff,T} \frac{\partial \overline{T}}{\partial x_j}\right] \tag{3.3}$$

in which:

$$\begin{cases} \mu_{eff,v} = \mu + \mu_{model} \\ \Gamma_{eff,T} = \mu/Pr + \mu_{model}/Pr_t \\ g_i = (-9.81, 0, 0) \end{cases} \tag{3.4}$$

μ_{model} and Pr_t depend on the turbulence model. These equations are used in the case of the Cartesian configurations, i.e. the infinite vertical channel, the cavity and the finite vertical channel. In the case of the finite vertical channel, these equations are solved assuming both constant and variable properties. When the variables are constant, Boussinesq approximation is applied. The Buoyancy force in this case is modeled using Equation 3.5.

$$-\frac{\partial \overline{P}}{\partial x_i} + \rho g_i = -\frac{\partial \overline{P}^*}{\partial x_i} - g_i \beta(\overline{T} - T_{ref}) \tag{3.5}$$

In the case of the variable property computations, it is assumed that the properties vary only as a function of temperature and Equation 3.2 is solved using no approximation.

3.1.2 Cylindrical coordinate system

In the case of the vertical cylinder configuration, for the sake of accuracy it is preferred to transfer the governing equations into cylindrical coordinate system. In this coordinate system, the equations not can be described in conservative form. The conservation equations read:

Continuity:

$$\frac{\partial \overline{u}}{\partial x} + \frac{1}{y}\frac{\partial y \overline{v}}{\partial y} + \frac{1}{y}\frac{\partial \overline{w}}{\partial \theta} = 0 \tag{3.6}$$

Material time derivative:

$$\mathbf{V} \cdot \nabla = \overline{u}\frac{\partial}{\partial x} + \overline{v}\frac{\partial}{\partial y} + \frac{1}{y}\overline{w}\frac{\partial}{\partial \theta} \tag{3.7}$$

The x-momentum equation:

$$\begin{aligned}&\frac{\partial \overline{u}}{\partial t} + (\mathbf{V}\cdot\nabla)\,\overline{u} = -\frac{1}{\rho}\frac{\partial \overline{p}}{\partial x} + g_x\beta(T - T_{ref}) + \\ &\frac{\partial}{\partial x}\left(\nu_{\mathit{eff}}\frac{\partial \overline{u}}{\partial x}\right) + \frac{1}{y}\frac{\partial}{\partial y}\left(y\nu_{\mathit{eff}}\frac{\partial \overline{u}}{\partial y}\right) + \frac{1}{y^2}\frac{\partial}{\partial \theta}\left(\nu_{\mathit{eff}}\frac{\partial \overline{u}}{\partial \theta}\right)\end{aligned} \tag{3.8}$$

The y-momentum equation:

$$\begin{aligned}&\frac{\partial \overline{v}}{\partial t} + (\mathbf{V}\cdot\nabla)\,\overline{v} - \frac{1}{y}\overline{w}^2 = -\frac{1}{\rho}\frac{\partial \overline{p}}{\partial y} + \frac{\partial}{\partial x}\left(\nu_{\mathit{eff}}\frac{\partial \overline{v}}{\partial x}\right) + \\ &\frac{1}{y}\frac{\partial}{\partial y}\left(y\nu_{\mathit{eff}}\frac{\partial \overline{v}}{\partial y}\right) + \frac{1}{y^2}\frac{\partial}{\partial \theta}\left(\nu_{\mathit{eff}}\frac{\partial \overline{v}}{\partial \theta}\right) - \nu_{\mathit{eff}}\frac{\overline{v}}{y^2} - \frac{2}{y^2}\nu_{\mathit{eff}}\frac{\partial \overline{w}}{\partial \theta}\end{aligned} \tag{3.9}$$

The θ-momentum equation:

$$\begin{aligned}&\frac{\partial \overline{w}}{\partial t} + (\mathbf{V}\cdot\nabla)\,\overline{w} + \frac{1}{y}\overline{v}\,\overline{w} = -\frac{1}{\rho y}\frac{\partial \overline{p}}{\partial \theta} + \frac{\partial}{\partial x}\left(\nu_{\mathit{eff}}\frac{\partial \overline{w}}{\partial x}\right) + \\ &\frac{1}{y}\frac{\partial}{\partial y}\left(y\nu_{\mathit{eff}}\frac{\partial \overline{w}}{\partial y}\right) + \frac{1}{y^2}\frac{\partial}{\partial \theta}\left(\nu_{\mathit{eff}}\frac{\partial \overline{w}}{\partial \theta}\right) - \nu_{\mathit{eff}}\frac{\overline{w}}{y^2} + \frac{2}{y^2}\nu_{\mathit{eff}}\frac{\partial \overline{v}}{\partial \theta}\end{aligned} \tag{3.10}$$

The energy equation:

$$\begin{aligned}&\frac{\partial \overline{T}}{\partial t} + (\mathbf{V}\cdot\nabla)\,\overline{T} = \\ &\frac{\partial}{\partial x}\left(\alpha_{\mathit{eff}}\frac{\partial \overline{T}}{\partial x}\right) + \frac{1}{y}\frac{\partial}{\partial y}\left(y\alpha_{\mathit{eff}}\frac{\partial \overline{T}}{\partial y}\right) + \frac{1}{y^2}\frac{\partial}{\partial \theta}\left(\alpha_{\mathit{eff}}\frac{\partial \overline{T}}{\partial \theta}\right)\end{aligned} \tag{3.11}$$

in which:

$$\begin{cases}\nu_{\mathit{eff}} = \nu + \nu_{model} \\ \alpha_{\mathit{eff}} = \nu/Pr + \nu_{model}/Pr_t\end{cases} \tag{3.12}$$

3.2 *RANS* Modeling

RANS simulations are both time and cost efficient for designing an experimental apparatus or finding the optimal operating conditions of the apparatus. In contrast, *LES* simulations are time consuming and sensitive to both the boundary conditions and grid resolution. Therefore performing *RANS* computations before *LES* simulations give a knowledge about the flow and the required mesh resolution. Besides, the acquired *RANS* results can be used as the initial boundary condition in the case of the *LES* computations which results in reaching to the state of numerically fully developed condition faster.

3.2.1 Turbulence model

The $k-\omega$ model of Peng *et al.* (1997) (hereafter *PDH* model) and $k-\varepsilon$ of Abe *et al.* (1994) (hereafter *AKN* model) were tested on a two dimensional square cavity and the results were compared with the *LES* results of Peng & Davidson (2001*b*) and the experimental results of Tian & Karayiannis (2000*a*).

It was found that the results of *PDH* model were in a better agreement with the experimental and the *LES* results compared to the *AKN* model. This was mainly due to the ability of the *PDH* model to predict the transition location compared to the *AKN* model.

Therefore from now on the *PDH* model is used to acquire the initial boundary conditions for all the study cases. This model is also used to design the operating conditions of the experimental apparatus (vertical cylinder configuration) and finding the proper and stable boundary conditions for the *LES* simulations.

The kinetic energy and specific dissipation equations of *PDH* model read:

$$(\mathbf{V}\cdot\nabla)\,k=\frac{\partial}{\partial x}\left(\nu_{\mathit{eff},k}\frac{\partial k}{\partial x}\right)+\frac{1}{y}\frac{\partial}{\partial y}\left(y\nu_{\mathit{eff},k}\frac{\partial k}{\partial y}\right)+P_k-C_k f_k\omega k \tag{3.13}$$

$$\begin{aligned}(\mathbf{V}\cdot\nabla)\,\omega=&\frac{\partial}{\partial x}\left(\nu_{\mathit{eff},\omega}\frac{\partial \omega}{\partial x}\right)+\frac{1}{y}\frac{\partial}{\partial y}\left(y\nu_{\mathit{eff},\omega}\frac{\partial \omega}{\partial y}\right)+\\&\frac{\omega}{k}(C_{\omega1}f_\omega P_k-C_{\omega2}\omega^2)+C_\omega\frac{\nu_t}{k}\left(\frac{\partial\omega}{\partial x}\frac{\partial\omega}{\partial x}+\frac{\partial\omega}{\partial y}\frac{\partial\omega}{\partial y}\right)\end{aligned} \tag{3.14}$$

The last two terms in the ω-equation are cross-diffusion terms. Other parameters and constants in the equations are:

$$\begin{cases}\nu_{\mathit{eff},\omega}=\nu+\nu_t/\sigma_\omega\\ \nu_t=C_\mu f_\mu k/\omega\\ f_\mu=0.025+\\ \qquad\left\{1-\exp\left[-\left(\frac{R_t}{10}\right)^{3/4}\right]\right\}\left\{0.975+\frac{0.001}{R_t}\exp\left[-\left(\frac{R_t}{200}\right)^2\right]\right\}\\ f_k=1-0.722\exp\left[-(R_t/10)^4\right]\\ f_\omega=1+4.3\exp\left[-(R_t/1.5)^{1/2}\right]\\ R_t=k/\nu\omega\\ C_\mu=1.0,\ C_k=0.09,\ C_{\omega1}=0.42,\ C_{\omega2}=0.075,\ C_\omega=0.75\\ \sigma_k=0.8,\ \sigma_\omega=1.35\end{cases} \tag{3.15}$$

In this model, the value of ω at the wall adjacent nodes is set to $\omega_{wall} = 6\nu/(C_{\omega 2} y_n^2)$ in which y_n is the normal distance of the node from the wall.

3.3 Large-Eddy Simulation

The Large-Eddy Simulation approach is a compromise between accuracy and CPU time compared to the conventional Reynolds Averaged Navier Stokes (RANS) and Direct Numerical Simulation methods. Since the turbulence has a three dimensional unsteady nature, it is believed that this method is appropriate to capture the unsteady effects of the turbulence. This is similar to *DNS* method but the grids in the case of the *LES* computations are fine enough to capture only the energy containing eddies or large eddies. The smaller eddies are modelled using a sub-grid scale (*SGS*) model.

This method is mainly used in this work to study the natural convection boundary layer on the vertical cylinder, in the cavity and in the finite vertical channel. In the case of the vertical channel only Smagorinsky *SGS* model (Smagorinsky, 1963) is used. In the case of the cavity, different *SGS* models are examined and it is found that the dynamic model of Germano *et al.* (1991) is the only model that predicts the location of the transition correctly and gives the best results in agreement to the measurements. Consequently in the case of the finite vertical channel, only the dynamic *SGS* model is employed to carry out the simulations.

The *SGS* models that have been employed in this work are explained in the following.

3.3.1 Smagorinsky (*SMG*) model

This *SGS* model is used in the cases of both the vertical cylinder configuration and the cavity configuration. The model, which was presented by Smagorinsky (1963), needs a damping function to correct the near-wall behaviour of the *SGS* viscosity. In this work the exponential damping function proposed by van Driest (1956) is used. In the case of the vertical cylinder, the model is transferred into cylindrical coordinate system. This model is described in both coordinate systems as follows.

***SMG* model in Cartesian coordinate system**

This model in the Cartesian coordinate system reads:

$$\begin{cases} \mu_{sgs} = \rho(C_S \Delta f_\mu)^2 \sqrt{2\overline{s}_{ij}\overline{s}_{ij}} \\ \Delta = (\Delta x \Delta y \Delta z)^{1/3} \\ \overline{s}_{ij} = \frac{1}{2}(\partial \overline{u}_i/\partial x_j + \partial \overline{u}_j/\partial x_i) \\ f_\mu = 1 - \exp\left(-y_n^+/25\right) \\ C_S = 0.1,\ Pr_t = 0.4 \end{cases} \tag{3.16}$$

μ_{sgs} takes the place of μ_{model} in Equation 3.4.

***SMG* model in cylindrical coordinate system**

In the cylindrical coordinate system the Smagorinsky model reads:

$$\begin{cases} \mu_{sgs} = \rho(C_S \Delta f_\mu)^2 \sqrt{2\overline{s}_{ij}\overline{s}_{ij}} \\ \Delta = (\Delta \mathcal{V})^{1/3} = (\Delta x \times \Delta y \times y \Delta \theta)^{1/3} \\ 2\overline{s}_{ij}\overline{s}_{ij} = 2\left[\left(\frac{\partial \overline{u}}{\partial x}\right)^2 + \left(\frac{\partial \overline{v}}{\partial y}\right)^2 + \left(\frac{1}{y}\frac{\partial \overline{w}}{\partial \theta} + \frac{\overline{v}}{y}\right)^2\right] + \\ \left[\left(\frac{1}{y}\frac{\partial \overline{v}}{\partial \theta} + \frac{\partial \overline{w}}{\partial y} - \frac{\overline{w}}{y}\right)^2 + \left(\frac{\partial \overline{v}}{\partial x} + \frac{\partial \overline{u}}{\partial y}\right)^2 + \left(\frac{\partial \overline{w}}{\partial x} + \frac{1}{y}\frac{\partial \overline{u}}{\partial \theta}\right)^2\right] \\ f_\mu = 1 - \exp\left(-\frac{y_n^+}{25}\right) \\ C_S = 0.1,\ Pr_t = 0.4 \end{cases} \tag{3.17}$$

This μ_{sgs} takes the place of μ_{model} in Equation 3.12.

3.3.2 WALE model

This model is proposed by Nicoud & Ducros (1999) and is capable of taking the effects of both the strain and rotation rate of the smallest resolved turbulent fluctuations into account. This model, which automatically recovers the correct proportionality of the SGS viscosity near walls ($\mu_{sgs} \propto y^3$), reads:

$$\begin{cases} \mu_{sgs} = \rho(C_\omega \Delta)^2 (\overline{s}_{ij}^d \overline{s}_{ij}^d)^{3/2} / \left[(\overline{s}_{ij}\overline{s}_{ij})^{5/2} + (\overline{s}_{ij}^d \overline{s}_{ij}^d)^{5/4}\right] \\ \overline{s}_{ij}^d = \frac{1}{2}(g_{ij}^2 + g_{ji}^2) - \frac{1}{3}\delta_{ij} g_{kk}^2 \\ g_{ij} = \partial \overline{u}_i/\partial x_j,\ g_{ij}^2 = g_{ik} g_{kj} \\ C_\omega = 0.33,\ Pr_t = 0.4 \end{cases} \tag{3.18}$$

This model is only used in the case of the cavity configuration.

3.3.3 Dynamic (*DYN*) model

According to Murakami (1997) the proposed dynamic model of Germano *et al.* (1991) together with the least square approach of Lilly (1992) is a very specific model which is capable of capturing the physics of both the stratified and transitional flows. Since the cavity configuration is characterized by both of the phenomena, this model is employed in this case and promising results are obtained. Since good results are obtained in this case, this model is also used in the case of the finite vertical channel.

This model dynamically computes the constant of the Smagorinsky by comparing two sets of spatially filtered Navier-Stokes equations. The applied spatial filters are based on the grid size (grid scale) and a coarser filter (test scale) that is twice as large as the grid size in this study. The consistency between the sub-grid stresses of the two filtered equations yields the local magnitude of the coefficient.

With regard to the grid scale stresses, i.e. $\tau_{ij} = \overline{u_i u_j} - \overline{u}_i \overline{u}_j$, and the test scale stresses, i.e. $T_{ij} = \widehat{\overline{u_i u_j}} - \widehat{\overline{u}}_i \widehat{\overline{u}}_j$, the modeled stresses read:

$$\begin{cases} \tau_{ij} - \frac{1}{3}\delta_{ij}\tau_{kk} = -2C_s\Delta^2|\overline{S}|\overline{S}_{ij} \\ T_{ij} - \frac{1}{3}\delta_{ij}T_{kk} = -2C_s\widehat{\Delta}^2|\widehat{\overline{S}}|\widehat{\overline{S}}_{ij} \\ \widehat{\Delta} = 2\Delta \end{cases} \tag{3.19}$$

The difference between the test scale and the test scale filter of the grid-scale stresses, i.e. $L_{ij} = T_{ij} - \widehat{\tau_{ij}} = \widehat{\overline{u_i}\overline{u_j}} - \widehat{\overline{u}}_i\widehat{\overline{u}}_j$, gives the resolved components of the stress tensor, which are associated with the scales of motion between the test and the grid scales or the so called test window scales. Using Equation 3.19, the associated stresses can be related and compared to the modeled stresses so that:

$$\begin{cases} L_{ij} - \frac{1}{3}\delta_{ij}L_{kk} = -2C_s M_{ij} \\ M_{ij} = \widehat{\Delta}^2|\widehat{\overline{S}}|\widehat{\overline{S}}_{ij} - \Delta^2\widehat{|\overline{S}|\overline{S}_{ij}} \end{cases} \tag{3.20}$$

Since Equation 3.20 represents five independent equations, there will consequently be five different C_s constants. Applying the least square concept to Equation 3.20, i.e. $\partial(L_{ij} - \frac{1}{3}\delta_{ij}L_{kk} + 2C_sM_{ij})^2/\partial C_s = 0$, C_s can be evaluated as follows:

$$C_s = -\frac{1}{2}(L_{ij}M_{ij}/M_{ij}^2) \tag{3.21}$$

The turbulent Prandtl number in this method, contrary to the other SGS models, is also calculated dynamically. Following a similar procedure for the temperature equation, it can be concluded that:

$$\begin{cases} C_t = -P_j R_j / R_j^2 \\ P_j = \widehat{\overline{u}_j \overline{T}} - \widehat{\overline{u}}_j \widehat{\overline{T}} \\ R_j = \widehat{\Delta}^2 |\widehat{\overline{S}}| \widehat{\frac{\partial \overline{T}}{\partial x_j}} - \Delta^2 \widehat{|\overline{S}| \frac{\partial \overline{T}}{\partial x_j}} \\ Pr_t = C_s / C_t \end{cases} \tag{3.22}$$

Although the averages of C_s and C_t in the cyclic direction are computed and applied at each iteration, it is observed that their values change drastically during the simulations. The violent behaviour of these constants, could potentially cause instability in the convergence process. To avoid possible divergence, the values of C_s and C_t are clipped to 0.5 and 1.25, respectively, whenever exceeded. In the case of the negative values, they are clipped such that $\mu_{sgs} + \mu \geq 0$ and $\mu_{sgs}/Pr_t + \mu/Pr \geq 0$.

3.4 Direct Numerical Simulation

Direct Numerical Simulation method (*DNS*) is the most accurate numerical method. In this method, even the smallest scales of turbulence should be simulated. It means that the size of the grid cells is in the order of Kolmogorov micro-scales. The drawback with this method is the need for very powerful computers with high memory capacities even in the case of simple geometries and flows.

The only case in this work which is studied using *DNS* is the infinite vertical channel. The governing Navier-Stokes and temperature equations in this case are non-dimensionalized. Equations 3.23 to 3.25 show the non-dimensional form of the continuity, momentum and energy equations.

$$\frac{\partial u_j}{\partial x_j} = 0 \tag{3.23}$$

$$\frac{\partial u_i}{\partial t} + \frac{\partial}{\partial x_j}(u_j u_i) = -\frac{1}{\rho}\frac{\partial p}{\partial x_i} + \frac{1}{Re}\frac{\partial^2 u_i}{\partial x_j \partial x_j} + \frac{Gr}{Re^2}(T - T_f)\delta_{1i} \tag{3.24}$$

$$\frac{\partial T}{\partial t} + \frac{\partial}{\partial x_j}(u_j T) = \frac{1}{Pr\,Re}\frac{\partial^2 T}{\partial x_j \partial x_j} \tag{3.25}$$

in which $Gr = 9.6 \times 10^5$ and $Re = 150$.

3.5 Numerical Procedure

In the case of the *RANS* computations a different numerical procedure is used compared to the *LES* and *DNS* simulations.

3.5.1 Numerical procedure for *RANS* computations

In this case the governing equations are solved in the steady state condition and a second order *QUICK* scheme for momentum equations and second order Van Leer scheme for turbulence models are used to discretize the governing equations (see Davidson & Farhanieh (1995) for further details).

The discretized equations are solved using the SIMPLEC algorithm and Rhie and Chow interpolation on a collocated grid arrangement.

3.5.2 Numerical procedure for *LES* and *DNS* simulations

In the case of the *LES* and *DNS* simulations, a conventional finite volume method is used to solve the three-dimensional continuity, Navier-Stokes and temperature equations. Implicit space filtering is applied to the equations with constant properties. However, Favre averaged equations are solved in the case of the variable properties. The numerical procedure is based on an implicit, fractional step technique with a multi-grid pressure Poisson solver (Emvin, 1997) and a non-staggered grid arrangement (Davidson & Peng, 2003).

The pressure Poisson equation in the case of the constant property equations reads:

$$\frac{\partial^2 P}{\partial x_i \partial x_i} = \frac{\rho}{\Delta t}\frac{\partial u_i^*}{\partial x_i} \tag{3.26}$$

where u_i^* is the intermediate velocity in the fractional step solution procedure (see Davidson & Peng (2003) for details) and Δt is the numerical time interval. In the variable property computations (finite vertical channel), considering the continuity equation, the Poisson equation for

pressure reads:

$$\frac{\partial^2 P}{\partial x_i \partial x_i} = \frac{1}{\Delta t}\left(\frac{\partial \rho}{\partial t} + \frac{\partial \rho u_i^*}{\partial x_i}\right) \tag{3.27}$$

The governing equations are discretized in time using the second-order Crank-Nicolson scheme.

As it is very important not to dissipate the turbulence by conventional numerical schemes, it is customary to discretize the governing equations by central difference scheme. Unfortunately, using central difference scheme in cells with the Peclet number $|Pe| > 2$ sometimes leads to generation of a so called unphysical or spurious fluctuations. In the literature this is usually called the wiggle problem. Once generated, these spurious fluctuations will soon propagate throughout the whole computational domain. To remedy this problem, a wiggle detector in combination with the central difference and Van-Leer scheme is used which is explained in the following section.

Wiggle detector

The problem with the pure central difference scheme is that this scheme is not bounded (see Versteegh & Malalasekera (1995)). This is the reason why spurious fluctuations are generated when pure central difference scheme is used. If a spurious fluctuation could be detected, it would be possible to use a bounded scheme like second order Van-Leer scheme to recalculate the flow parameters in that cell. This scheme is blended with the central difference scheme with deferred correction of Ferziger & Peric (1996) to discretize the governing equations. The resulting scheme can simply be shown as:

$$\dot{m} u_{UDS}^n + \dot{m}\left[\alpha u_{CDS}^{n-1} - \alpha u_{UDS}^{n-1} + (1-\alpha) u_{UDS_{corr}}^{n-1}\right] \tag{3.28}$$

In Equation 3.28, CDS, UDS and UDS_{corr} stand for the central difference scheme, 1st-order upwind scheme and 2nd-order correction to the lower order upwind scheme, respectively. n and $n-1$ stand for current and previous iterations, respectively, and α is a blending factor which can take a value equal to zero or one. $\alpha = 0$ gives Van-Leer scheme and $\alpha = 1$ gives central difference scheme with deferred correction. The idea is to set $\alpha = 0$ when a wiggle is detected and $\alpha = 1$ otherwise. As the Van-Leer scheme is bounded, the wiggle will be removed.

In the case of the temperature, it is easy to detect the spurious fluctuations. In the absence of source terms, the temperature in a cell can not be higher or lower than the neighbouring cells. At the same time, the cell temperatures can not be smaller or higher than the minimum and maximum boundary values, respectively. In the case of the velocities, however, it is not an easy task to define the difference between a numerical wiggle and a turbulent fluctuation. So it may happen that the turbulence is dampened instead of removing the wiggles as the Van-Leer scheme is too dissipative for *LES* fluctuations. For the velocities, the proposed method by Mary & Sagaut (2002) and Dahlström & Davidson (2003) is used to detect the unphysical wiggles. Accordingly, the definition of wiggle is depicted in Figure 3.1.

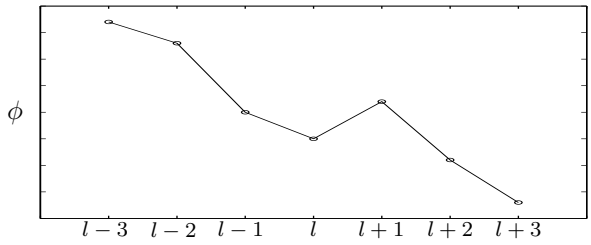

Figure 3.1: Wiggle definition.

The wiggle will be detected at the $l + 1/2$ face when the following correlations are satisfied:

$$\begin{cases} (\phi_{l+1} - \phi_l)(\phi_l - \phi_{l-1}) < 0 \\ \qquad \text{and} \\ (\phi_{l+2} - \phi_{l+1})(\phi_{l+1} - \phi_l) < 0 \end{cases} \tag{3.29}$$

Here, ϕ stands for a velocity component.

3.6 Radiation Heat Transfer

In the case of the finite vertical channel configuration, the temperature of the heated wall increases considerably. Due to this temperature increase, the radiation heat transfer must be taken into account. The radiation heat transfer is assumed to be two-dimensional and, to calculate the amount of radiation exchange, the channel walls are segmented as it is shown in Figure 3.2. The strips are assumed to be infinite in the span-wise direction. In this figure, l and r stand for the

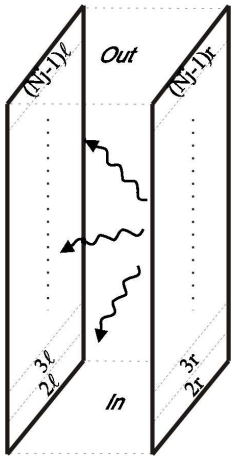

Figure 3.2: Schematic diagram of the radiation heat transfer in the channel.

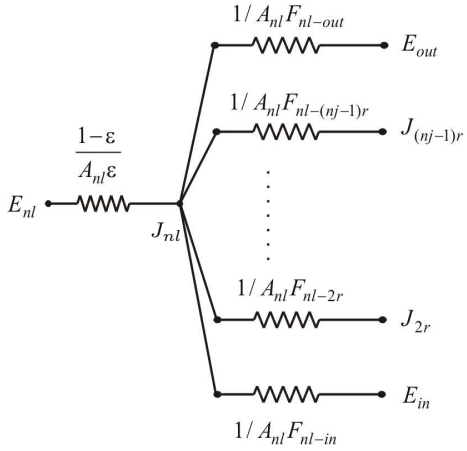

Figure 3.3: Equivalent circuit diagram of the radiation heat transfer in the channel.

left and the right wall respectively and $nj-1$ is the number of cells in the stream-wise direction.

The equivalent circuit diagram of the radiation exchange between the n^{th} strip on the left wall ($n = 2...nj-1$), the right wall strips, the inlet and the outlet is shown in Figure 3.3. The inlet and the outlet are assumed to be black bodies and the area weighted average temperature at each surface is assumed to be the temperature of the surface.

By considering this diagram for the left or insulated wall and a similar diagram for the right or heated wall, Equations 3.30 and 3.31 show the equations for the left and the right wall cell radiosities, J_{nl} and J_{nr}, respectively.

$$J_{nl}\left(\tfrac{1}{1-\varepsilon}\right) - \sum_{m=2}^{nj-1}\left(J_{mr}F_{nl-mr}\right) = E_{nl}\left(\tfrac{\varepsilon}{1-\varepsilon}\right) + E_{out}F_{nl-out} + E_{in}F_{nl-in} \tag{3.30}$$

$$J_{nr}\left(\tfrac{1}{1-\varepsilon}\right) - \sum_{m=2}^{nj-1}\left(J_{ml}F_{nr-ml}\right) = E_{nr}\left(\tfrac{\varepsilon}{1-\varepsilon}\right) + E_{out}F_{nr-out} + E_{in}F_{nr-in} \tag{3.31}$$

In the equations, F_{nl-mr} is the view factor between the n^{th} strip on the left wall and m^{th} strip on the right or heated wall, $\varepsilon = 0.125$ is the emissivity of the walls and $E = \sigma T^4$ is the black body emission of a segment under which the name of the segment is written as the subscript.

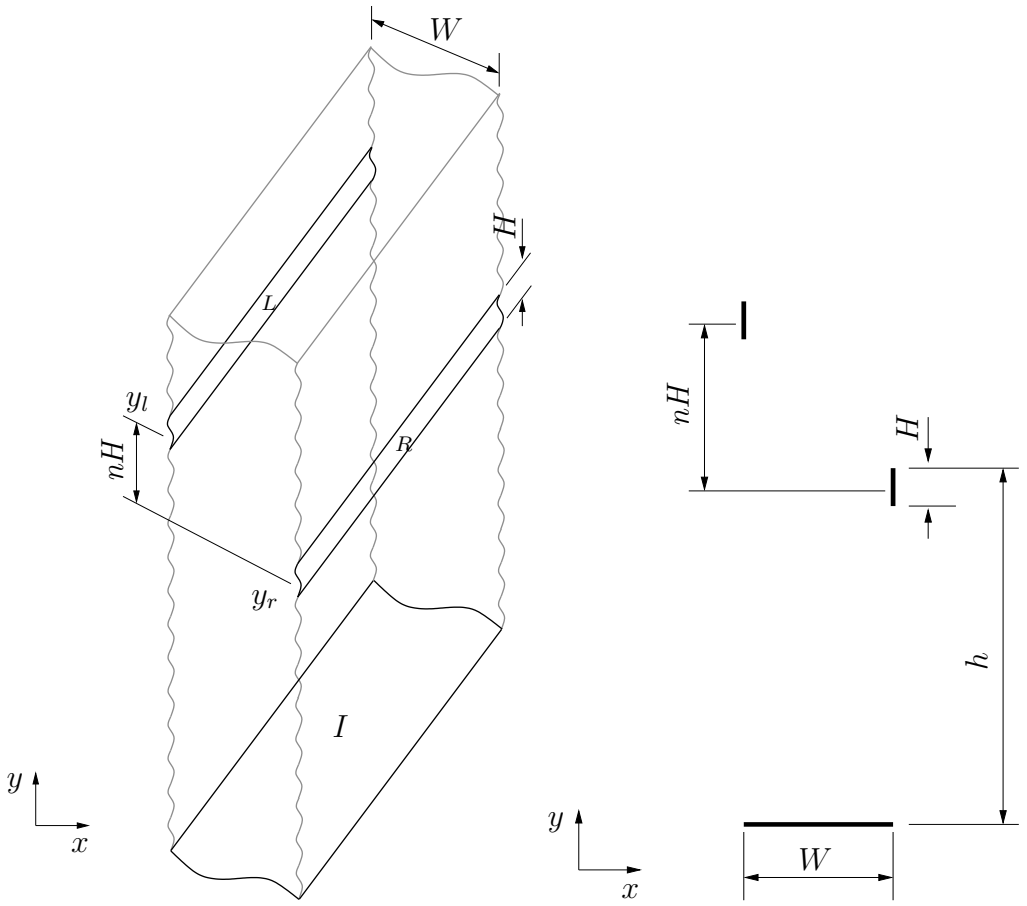

(a) Three dimensional configuration. (b) Two dimensional configuration.

Figure 3.4: The geometrical dimensions between the channel wall segments (strips) to calculate the view factor between them and the channel inlet and outlet.

Regarding Figure 3.4, view factors between the channel wall strips (considering two dimensionality) are calculated as:

$$\begin{cases} F_{R-L} = \frac{\sqrt{(n+1)^2\ A^2+1}-2\sqrt{n^2\ A^2+1}+\sqrt{(n-1)^2\ A^2+1}}{2A} \\ A = H/W,\ n = |y_r - y_l|/H \end{cases} \tag{3.32}$$

$$\begin{cases} F_{R-I} = \frac{W}{H}\left[\left(\frac{A-\sqrt{1+A^2}}{2}\right) - \left(\frac{A'-\sqrt{1+A'^2}}{2}\right)\right] \\ A = h/W,\ A' = (h-H)/W \end{cases} \tag{3.33}$$

Equations 3.30 and 3.31 are composed of $2 \times (nj - 1)$ equations that are solved by a Gauss-Seidel method at each time step. Provided the radiosities, the radiated and irradiated heat fluxes at each time step can be calculated using Equation 3.34.

$$\begin{cases} q''^{\,irrad}_{nl} & = \frac{E_{nl} - J_{nl}}{(1-\varepsilon)/\varepsilon} \\ q''^{\,rad}_{nr} & = \frac{E_{nr} - J_{nr}}{(1-\varepsilon)/\varepsilon} \end{cases} \tag{3.34}$$

The irradiated heat flux will be used as the actual heat flux of the left wall (instead of the zero value) and the radiated heat flux will be subtracted from q''_w to account for the effect of the radiation heat transfer.

The accuracy of this model was examined in a two dimensional geometry similar to Figure 2.9 assuming no fluid flow, constant wall temperatures and black body radiation exchange between the surrounding (inlet and outlet) and the channel walls. The error was within 1% with respect to the analytical solution.

Chapter 4

Summary of Results

The results of this work are shown and presented in the attached papers. A summary of the results of these papers and those results which are not published will be given here.

4.1 Natural Convection Boundary Layer on Vertical Cylinder

As mentioned earlier, the operating conditions of the experimental apparatus which consists of two concentric vertical cylinders (inner cylinder heated and the outer one is insulated) is studied using *RANS* simulations. The results are published in *Paper I*. The acquired numerical results together with the suggested boundary conditions are used to carry out the *LES* simulations. In this section, the results of the case with $\theta = 126^o$ are shown.

Since the grid is coarse near the outer cylinder, it is necessary to use the wiggle detector in the *LES* simulations. Figure 4.1 shows the time-averaged blending factors of the Van-Leer (hereafter *VL*) and central difference with deferred correction (hereafter *CDDC*) schemes for velocities and temperature. In these figures, $\langle \alpha' \rangle = 0$ and $\langle \alpha' \rangle = 1$ represent the pure VL and the pure CDDC schemes respectively.

It can be seen in the figures that the most affected direction is the radial direction (y) and thus most of the wiggles are detected in this direction. This is probably due to the spatial resolution of the grid in this direction which is not fine enough to eliminate wiggle generation.

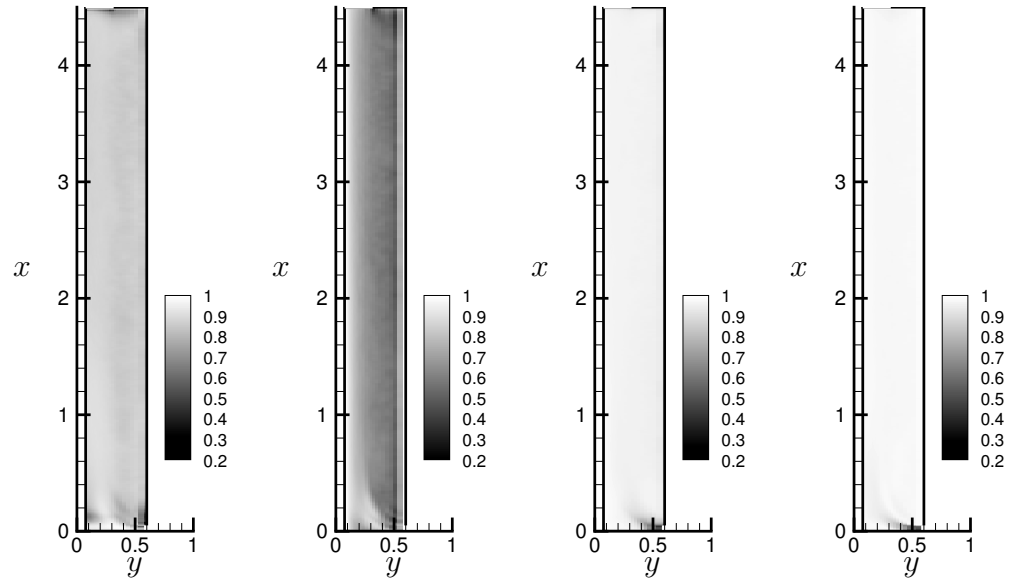

(a) $\langle \alpha'_x \rangle$. (b) $\langle \alpha'_y \rangle$. (c) $\langle \alpha'_\theta \rangle$. (d) $\langle \alpha'_t \rangle$.

Figure 4.1: Contours of time-averaged blending factor, $\langle \alpha' \rangle$.

However, for the other two directions and the temperature variable, it can be observed that except for the inlet region, the dominant scheme is the central difference scheme. Even in the y-direction, regions close to the inner hot tube are not strongly affected by wiggles.

Analysis of the results shows the existence of two recirculating regions one near the bottom of the experimental rig close to the inlet and another one near the outlet. These are shown in Figure 4.2.

Both of the circulation regions are caused by the sudden rush of the flow towards the inner cylinder or outlet. Owing to the acceleration of the flow towards the outlet, the results of this region, i.e. $Gr \geq 3.7 \cdot 10^{11}$ or $x/H \geq 0.9$, are not as reliable as the results of the rest of the domain in the sense that the natural convection might not be the dominant phenomenon in this region.

The recirculation region near the inlet triggers the onset of the turbulent regime at the very low heights on the inner vertical cylinder. This can be understood easily by examining Figure 4.3.

The Nusselt number starts already to deviate from the results of the laminar boundary layer at $x \geq 0.12m$ or $Ra \geq 5.7 \times 10^6$ whereas the transition in the case of the natural convection boundary layer on the flat

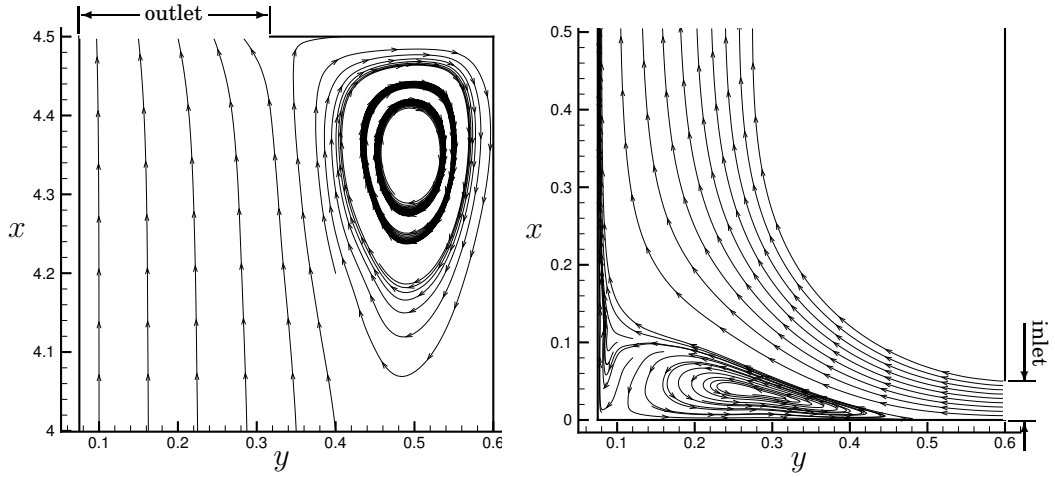

(a) Outlet region. (b) Inlet region.

Figure 4.2: Flow near the outlet and the inlet.

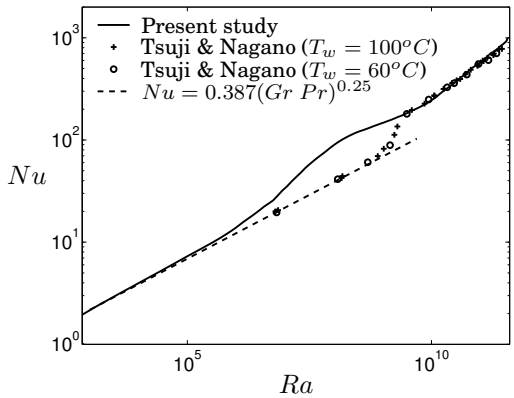

Figure 4.3: Nusselt number as a function of Rayleigh number.

plate starts from $Ra = 8 \cdot 10^8$ (results from Tsuji & Nagano (1988*a*)).The difference is probably due to first the turbulent inlet boundary condition, second, inherent differences between the characteristics of the natural convection boundary layer along a vertical flat plat and a vertical slender cylinder and third, existence of the outer shell which embraces the whole cylinder and provokes instabilities by creating some recirculating flows in the proximity of the boundary layer.

Although there exists a forced convected flow at the inlet of the vertical cylinder configuration, it should be mentioned that the effect of this flow compared to the natural convected flow is rather weak. This can be seen more clearly in Figure 4.4 in which the *2D* vector plots of the velocities in the entrance region and near the outlet are shown.

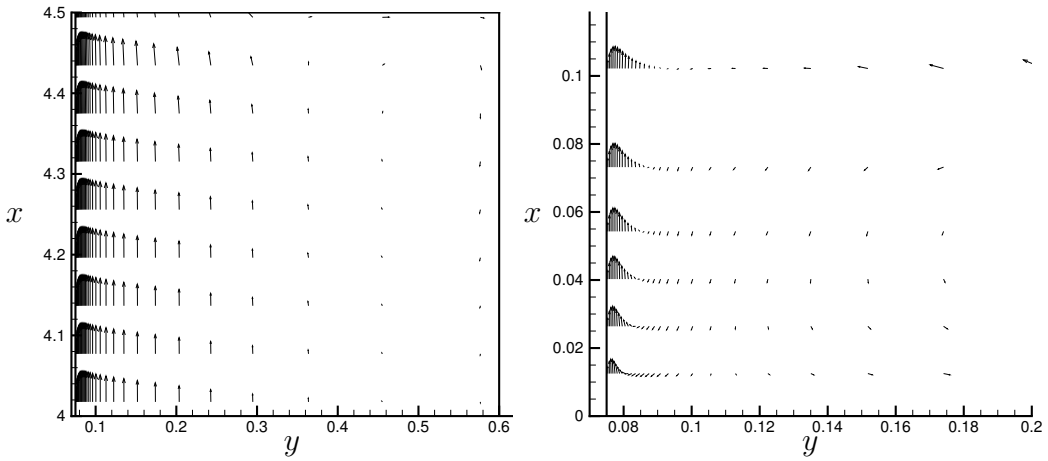

(a) Outlet region.

(b) Inlet region.

Figure 4.4: Vector plots of the flow near the outlet and inlet.

The velocity and temperature profiles in the laminar region are compared with the similarity solution results of Ostrach (1952) for a vertical flat plate. Close to the wall the results are in complete agreement, however, discrepancies become larger farther away from the wall. This is probably due to first the curvature of the cylinder that causes different boundary layer growth and second the existence of a secondary flow in the outer part of the boundary layer (see Figure 4.2(b)) which is in contrast to a perfect natural convection boundary layer in which case the flow is quiescent far from the boundary layer.

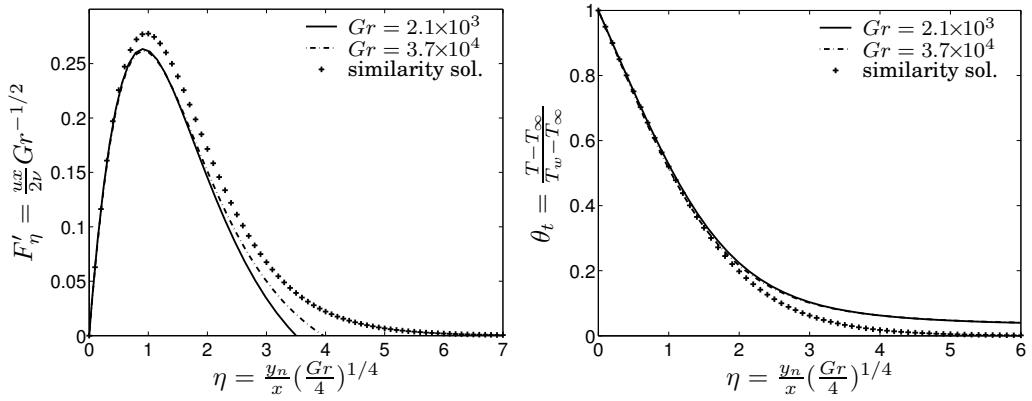

(a) Velocity profiles.

(b) Temperature profiles.

Figure 4.5: Comparison of velocity and temperature profiles with the similarity solution results in the laminar region.

Mean flow quantities and time averaged Reynolds stresses of the flow are obtained using 15000 time steps. Time interval in the *LES* simulations is set to $\Delta\tau = 2.27 \times 10^{-3} sec$. Considering Equation 4.1 which is the autocorrelation for a set of data with constant time interval, $\Delta\tau$:

$$R_j^\phi(j\Delta\tau) = \frac{\sum_{i=1}^{N-j} \phi'_i \phi'_{i+j}}{N-j}, \quad j = [0..N-1] \tag{4.1}$$

the integral time scale for a variable ϕ, is defined as the area below the autocorrelation curve which reads:

$$T_{int}^\phi = \int \frac{R_j^\phi}{R_0^\phi} d\tau \tag{4.2}$$

Autocorrelation curves for the stream-wise velocity and temperature are shown in Figures 4.6(a) and 4.6(b), respectively. The maximum integral time scale for the stream-wise velocity (u) and temperature autocorrelation curves are $T_{int}^u = 0.15 sec$ and $T_{int}^t = 0.07 sec$, respectively. Based on these values, approximately 230 independent samples are used to calculate the mean flow and turbulence parameters (see Appendix A). These estimated times also suggest that for obtaining uncorrelated data, the minimum time interval between each two contiguous samples should be $0.3 sec$.

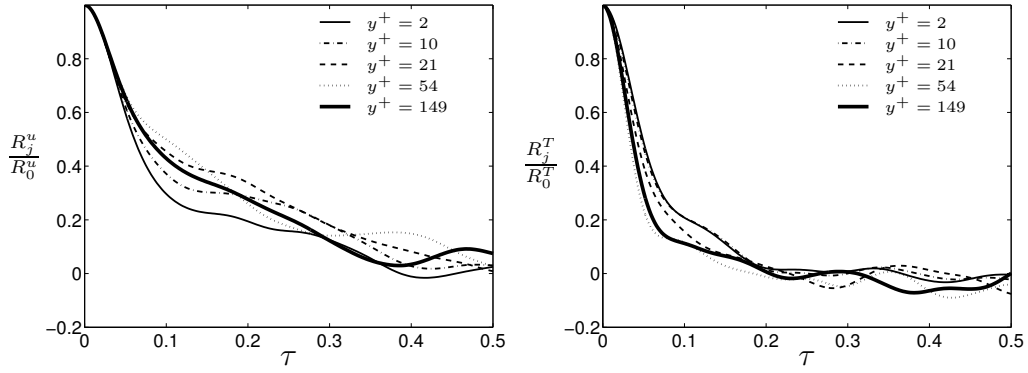

(a) u-autocorrelation curve.

(b) T-autocorrelation curve.

Figure 4.6: Autocorrelation curves at $Gr = 2.1 \cdot 10^{11}$.

4.1.1 Energy spectra

One way to check whether or not the grid is fine enough for the numerical computations is to check the cut-off location of the energy spectrum. The cut-off should take place in the inertial subrange for the *LES* computations. One-dimensional spectrum $E_{ij}(\kappa)$ in the x_i direction is defined to be *twice* the one-dimensional Fourier transform of the two-point correlation, R_{ij} (Pope, 2000):

$$E_{ij}(\kappa_k) \equiv \frac{1}{\pi} \int_{-\infty}^{\infty} R_{ij}(\mathbf{e_k} x_k) e^{-i\kappa x_k} dx_k \tag{4.3}$$

Energy spectra for velocity and temperature fluctuations in a region close to the wall are shown in Figure 4.7. For details on how the energy spectra are calculated see Appendix B. As can be seen in the figures, the cut-off has taken place well beyond the range where energy spectra are proportional to κ^{-3}. This is a region that is believed to follow immediately the inertial subrange, where $E \propto \kappa^{-5/3}$ (Peng & Davidson, 2002).

However, contrary to high Reynolds number forced convection boundary layer flows, the extent of the inertial subrange region is very small. In fact for the radial velocity it looks like a single point instead of a region. This difference between the natural convection boundary layer and forced convection boundary layers is probably due to the low Reynolds number characteristic of natural convection flows which

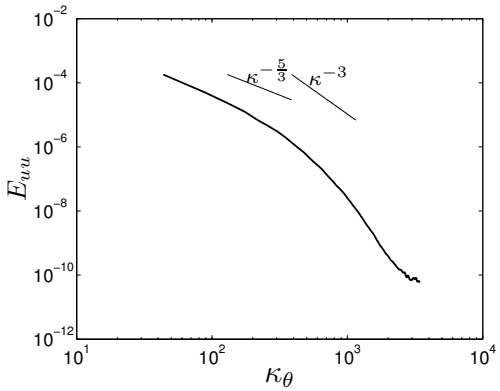

(a) Axial velocity energy spectrum.

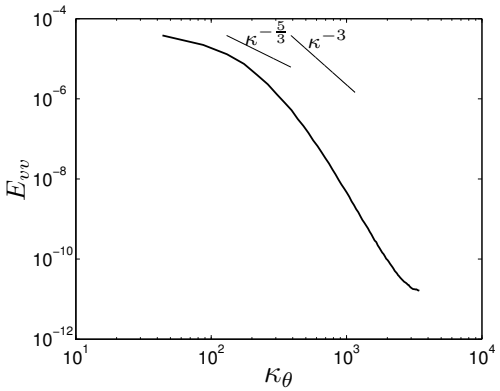

(b) Radial velocity energy spectrum.

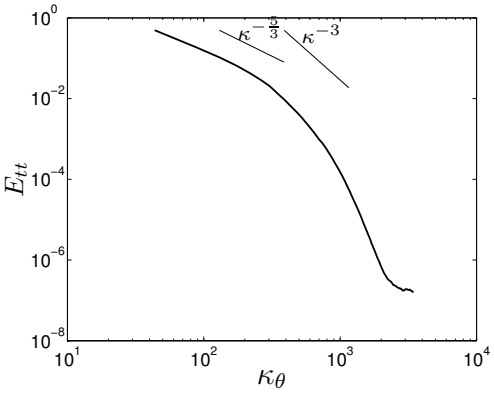

(c) Temperature energy spectrum.

Figure 4.7: One dimensional energy spectra at y^+=59, Gr=$1.8 \cdot 10^{11}$.

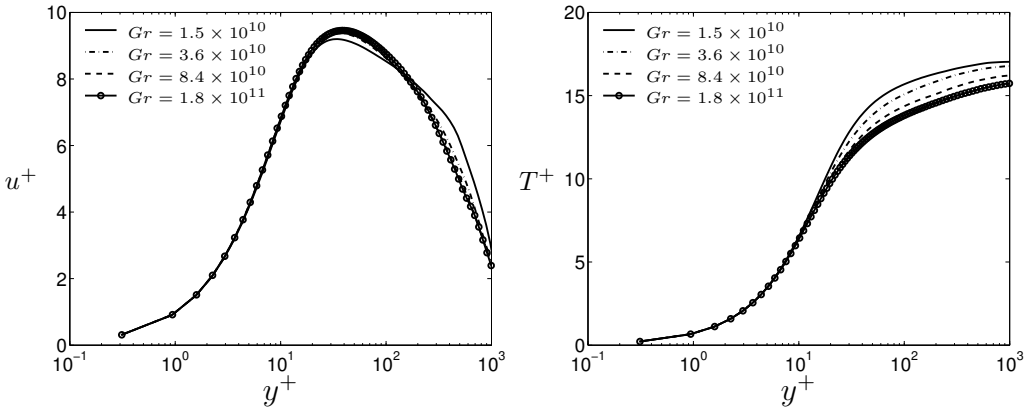

(a) Dimensionless velocity.

(b) Dimensionless temperature.

Figure 4.8: Mean velocity and temperature profiles.

makes the separation of scale to be less distinct than for high Reynolds number flows.

4.1.2 Mean flow parameters

Figure 4.10 shows the velocity and temperature profiles at different Grashof numbers.

For the reader's convenience, the relationship between the local Grashof number and cylinder height is shown in Figure 4.9.

Figure 4.10 shows that the profiles of the velocity collapse and exhibits

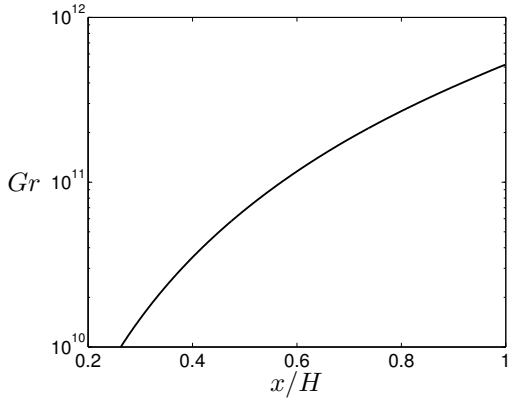

Figure 4.9: Local Grashof number variation versus cylinder height.

a self-similar behavior. However, this is not the case for the temperature profiles. This behaviour can be explained by the fact that the friction velocity makes the profiles collapse in the inner part of the boundary layer. This region is the so called constant heat flux layer and consists of a conductive, a thermo-viscous and a buoyant sublayer (George & Capp, 1979). It can be seen that this scaling is not appropriate for the outer part of the thermal boundary layer.

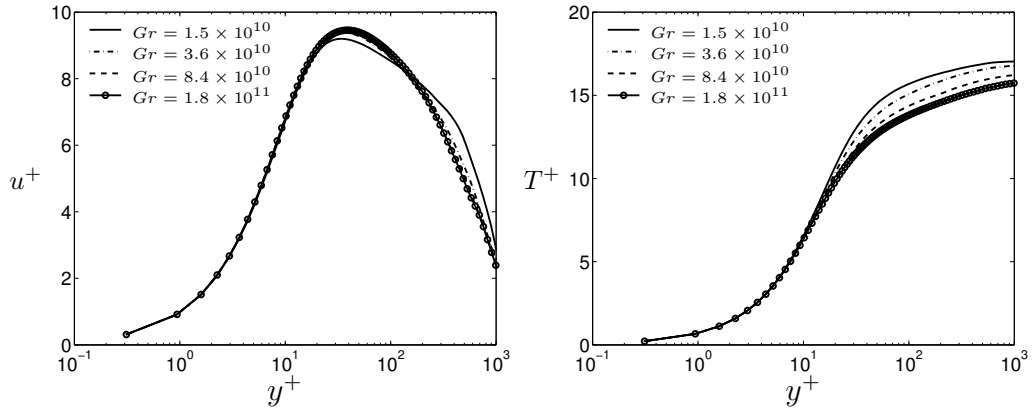

(a) Dimensionless velocity.

(b) Dimensionless temperature.

Figure 4.10: Mean velocity and temperature profiles.

4.1.3 Turbulence parameters

Figure 4.11 compares the predicted normal Reynolds stresses with the measurements of Tsuji & Nagano (1988*b*) and Persson & Karlsson (1996). As can be seen, temperature fluctuations acquire the largest peaks for both the simulations and the experimental results of Tsuji & Nagano (1988*b*). However, this is not the case for the measurements of Persson & Karlsson (1996) in which case the stream-wise normal stress has the largest peak. A comparison between present work and Tsuji & Nagano (1988*b*) results shows that the velocity and temperature fluctuations are qualitatively in good agreement and the locations of the peaks almost match each other. However, predicted temperature fluctuations are almost always larger than the experimentally measured values. Also, in Figure 4.11(a) the measured wall-normal Reynolds stress, shows a strange behavior in the region $7.5 < y^+ < 40$. Such region in which the measured wall-normal Reynolds stress seems

to have constant values, can not be observed in the case of the simulations.

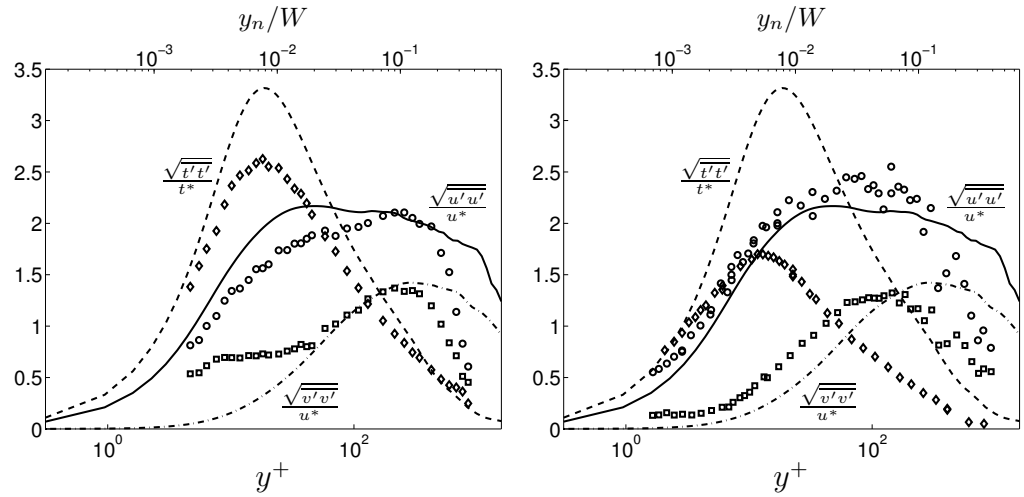

(a) Experimental data from Tsuji & Nagano (1988*b*), $Gr = 8.99 \cdot 10^{10}$.

(b) Experimental data from Persson & Karlsson (1996), $Gr = 1 \cdot 10^{10}$.

Figure 4.11: Normal stresses and temperature fluctuations. Lines: simulation, $Gr = 8.9 \cdot 10^{10}$; markers: experiments.

In Figure 4.11(b), except for the wall-normal Reynolds stress, discrepancies between the simulation and the experimental results of Persson & Karlsson (1996) are even larger. The location of the peaks in the experimental results except for the stream-wise normal stress, are closer to the wall compared to those of the computations. The measured wall-normal stress shows almost the same behavior as the computed one.

Figure 4.12 compares the normalized resolved shear stress ($\overline{u'v'}/u^{*2}$), stream-wise turbulent heat flux ($\overline{u't'}/u^*t^*$) and wall-normal turbulent heat flux ($\overline{v't'}/u^*t^*$) with the measurements of Persson & Karlsson (1996) and Tsuji & Nagano (1988*b*).

As can be seen in Figure 4.12(a), the wall-normal heat flux is almost in perfect agreement with the measured values. Stream-wise heat flux and Reynolds shear stress are also qualitatively in agreement with the measurements and the location of the maxima match each other fairly well. Although both the measured and predicted shear stress become zero near the wall in the region $y^+ < 4$, the existence of a region with negative shear stress is not confirmed by measurements whereas it exists in the simulations. The existence of such a negative region for Reynolds shear stress can not only be seen in the measure-

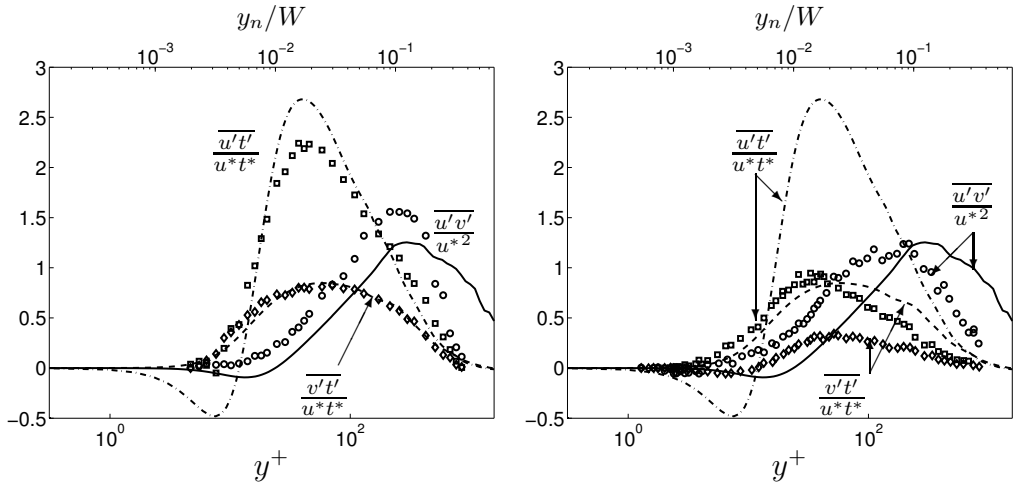

(a) Experimental data from Tsuji & Nagano (1988*b*), $Gr = 8.99 \cdot 10^{10}$.

(b) Experimental data from Persson & Karlsson (1996), $Gr = 2 \cdot 10^{10}$.

Figure 4.12: Turbulent shear stress and heat fluxes. Lines: simulation, $Gr = 8.9 \cdot 10^{10}$; markers: experiments.

ments of Persson & Karlsson (1996), but also it is previously reported by Miyamoto *et al.* (1982) and Cheesewright & Ierokipiotis (1984).

For the shear stress and the heat fluxes, discrepancies between simulation and measurements in Figure 4.12(b) are quite large. In this figure, contrary to Figure 4.12(a), the peak of the measured shear stress is larger than those of the stream-wise and wall-normal turbulent heat fluxes. Also, a negative region for the measured wall-normal heat flux exists which can be observed neither in the simulation nor in the Tsuji & Nagano (1988*b*) measurements. However, the negative stream-wise heat flux region that was confirmed by both the simulation and measurements of Tsuji & Nagano (1988*b*) can not be observed in the results of Persson & Karlsson (1996).

The credibility of the near wall measurements can be more investigated by considering the cross correlation coefficient which is defined in Equation 4.4.

$$R_{uv} = \frac{\overline{u'v'}}{\sqrt{\overline{v'^2}} \times \sqrt{\overline{u'^2}}} = \frac{\mathcal{O}(y^3)}{\sqrt{\mathcal{O}(y^4)} \times \sqrt{\mathcal{O}(y^2)}} = Cte. \tag{4.4}$$

From the Taylor expansion, and by applying the no-slip boundary condition and considering continuity equation, it can be found that close to the wall when y approaches zero, the cross correlation coefficient

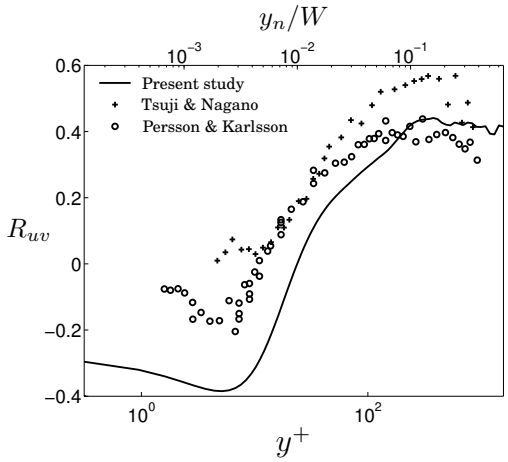

Figure 4.13: Cross correlation coefficient comparison.

(R_{uv}) approaches a constant value. This coefficient is plotted for the computed data and the existing measurements in Figure 4.13.

In the case of the measured values by Tsuji & Nagano (1988*b*), it can be seen that the curve has a local discontinuity close to $y^+ \approx 6$. Considering the computed results and the measurements of Persson & Karlsson (1996) it can be speculated that in the case of the data of Tsuji & Nagano (1988*b*) the curve shows a reversed behavior which can be caused by the hot-wire measurements that are incapable of realizing the flow direction.

4.2 Natural Convection Boundary Layer in Infinite Vertical Channel

In this case *DNS* computations are carried out. In fact this approach is the same as the *LES* with the difference that no *SGS* model is employed and the grid cell sizes are of the order of the Kolmogorov micro-scales.

As mentioned earlier, the main objective of this study is to understand to what extent the computational results are dependent on the computational domain.

To check the location of the cut-off and therefore the validity of DNS simulation, the result of one-dimensional energy spectrum for both stream-wise velocity and temperature fluctuations at a location near the wall and in the middle of the channel are shown in Figure 4.14.

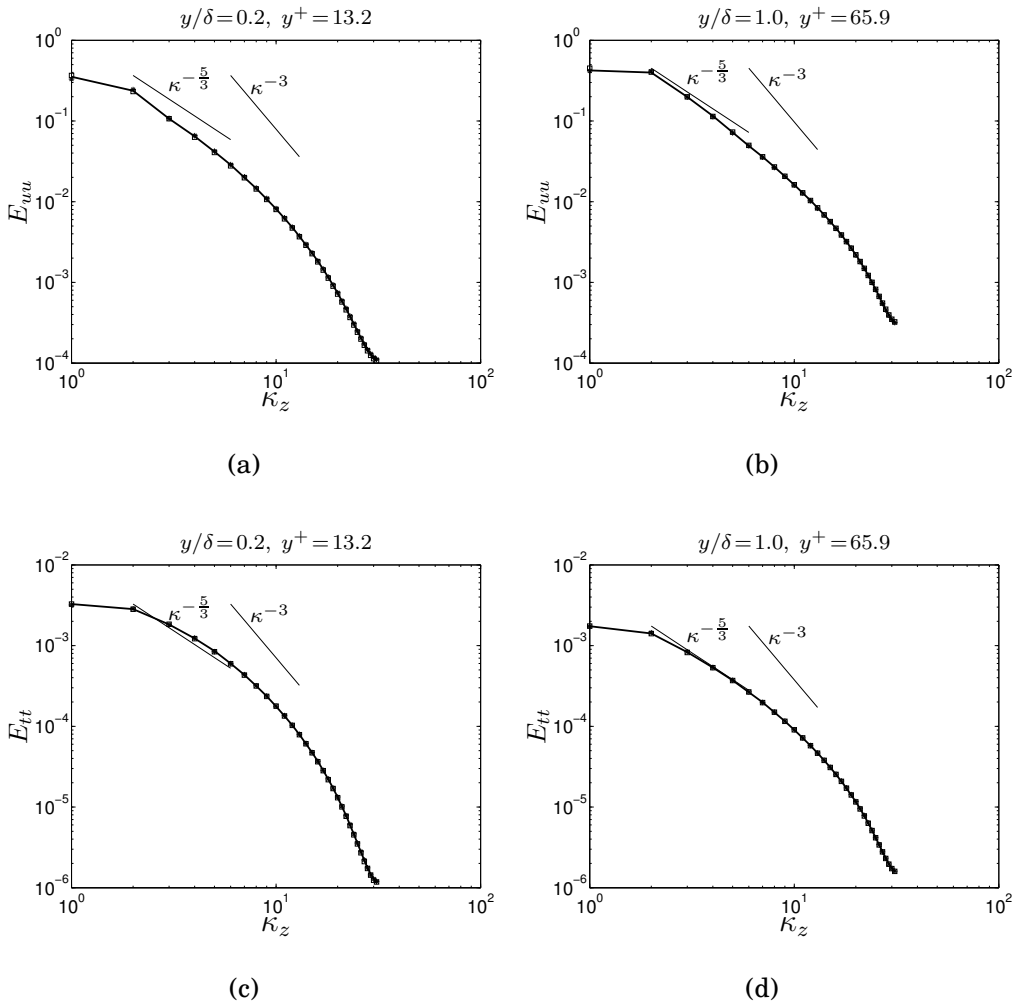

Figure 4.14: One dimensional energy spectra. Solid lines: $L = 7.6\pi$; squares: $L = 12\pi$; asterisks: $L = 18\pi$.

As it can be observed from the figures, all three lines almost perfectly match each other. The cut-off occurs well beyond the inertial subrange where the energy spectrum is proportional to $\kappa^{-5/3}$. For buoyancy dominated thermal flows, it is believed that the inertial subrange is followed by a so-called buoyancy subrange where the energy proportionality to wave number is κ^{-3} (Kotsovinos (1991) and Peng & Davidson (2002)).

4.2.1 Mean flow properties

The mean velocity and temperature profiles for the three computational domains are shown in Figure 4.15. As can be seen, no difference can be observed. An inspection of the velocity profiles confirms their perfect antisymmetric behavior.

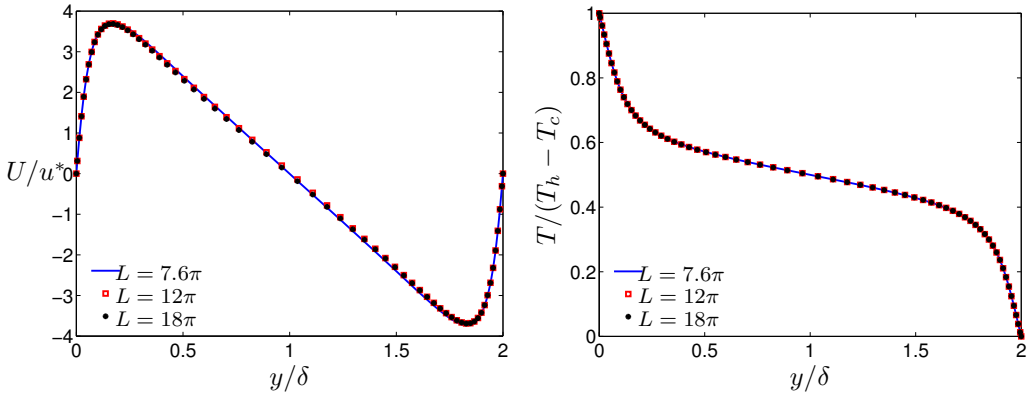

(a) Velocity profile.

(b) Temperature profile.

Figure 4.15: Mean profiles.

4.2.2 Turbulent parameters

Normal and shear stresses are shown in figures 4.16(a) and 4.16(b), respectively. Ignoring very small differences between stream-wise stresses, all stresses are in good agreement with each other.

The difference between forced and natural convecting flows can clearly be seen in the shear stress behavior. In channel flow with forced convection, shear stress acquires its maximum and zero values near the walls and at the center of the channel, respectively. However, in the

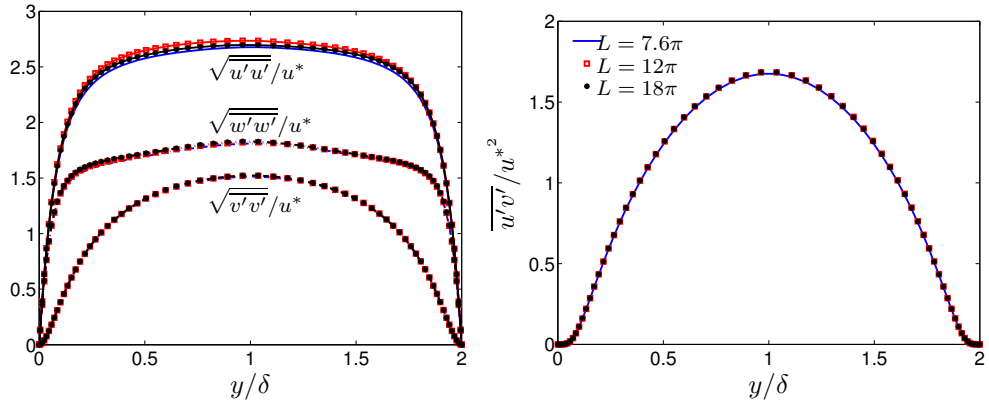

(a) Normal stresses.

(b) Turbulent shear stress.

Figure 4.16: Normalized resolved Reynolds stresses.

channel flow with mixed or natural convection, the buoyancy term influences the shear stress in such a way that it takes its maximum value at the center in the case of the pure natural convecting flow. In the case of mixed convection, the shear stress becomes smaller near the hot (buoyancy aiding) wall and larger near the cold (buoyancy opposing) wall (Davidson *et al.*, 2003).

Figures 4.17(a) and 4.17(b) show the turbulent heat fluxes and temperature fluctuations, respectively. Again very small differences can be observed between the results of the three different geometries. The stream-wise turbulent heat flux is larger than the wall-normal turbulent heat flux although the stream-wise gradient of the mean temperature is zero.

A comparison of the results of the turbulent stresses and heat fluxes (Figures 4.16 and 4.17) shows that the results are independent of the computational domain.

4.3 Natural Convection Boundary Layer in Cavity with Aspect Ratio $AR = 5$

This test case is an important case since all the three regions of laminar, transition and turbulent flow exist. Existence of the transition region makes the simulations highly sensitive to the grid resolution

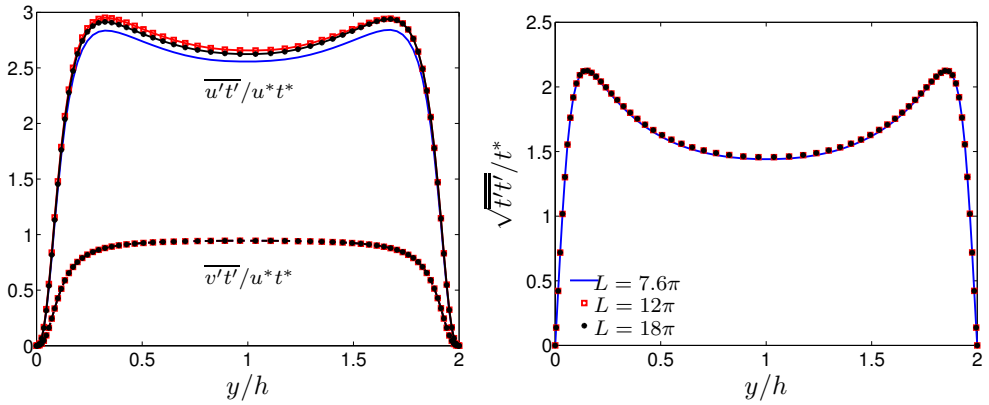

(a) Turbulent heat fluxes.

(b) Temperature fluctuations.

Figure 4.17: Resolved turbulent heat fluxes and temperature fluctuations.

and *SGS* model.

Figure 4.18 shows the contours of the velocity magnitude in the cavity. It can be seen that the flow accelerates up to the middle height of the cavity from where it begins to decelerate because of the existence of the upper and the lower horizontal walls. Hence some part of the flow returns and continues towards the other vertical wall. These movements generate the two high velocity regions which are not attached to the walls.

When the flow reaches the top (bottom) wall, it relaminarizes so that a fully laminar flow reaches the cold (hot) wall. However, if the top (bottom) wall is not perfectly insulated, the fluid loses heat and the relaminarization process will be hindered due to reduced stratification. Since making a perfect insulation in the experiments is very difficult, experimental results of Cheesewright *et al.* (1986) are asymmetric.

4.3.1 Mean flow parameters

Variations of C_f and Nu for the fine grid are shown in Figure 4.19. The *DYN* model shows the best agreement with the experimental results in the cases of both the friction coefficient and the Nusselt number. This agreement between the computed and measured results exists for heights up to $x = 1.5m$ from where the experimental and numerical results deviate from each other. This is probably related to the imperfect

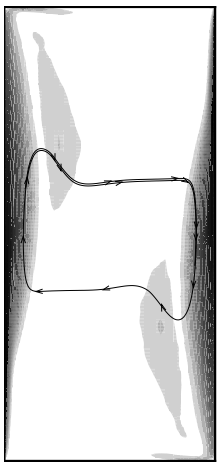

Figure 4.18: Contours of the velocity magnitude. Figure is not to scale.

insulation of the top wall in the experiment.

In this case, *DNS* means that no *SGS* model is used in the simulations. The grid resolution for this computation is probably too coarse to yield good accuracy.

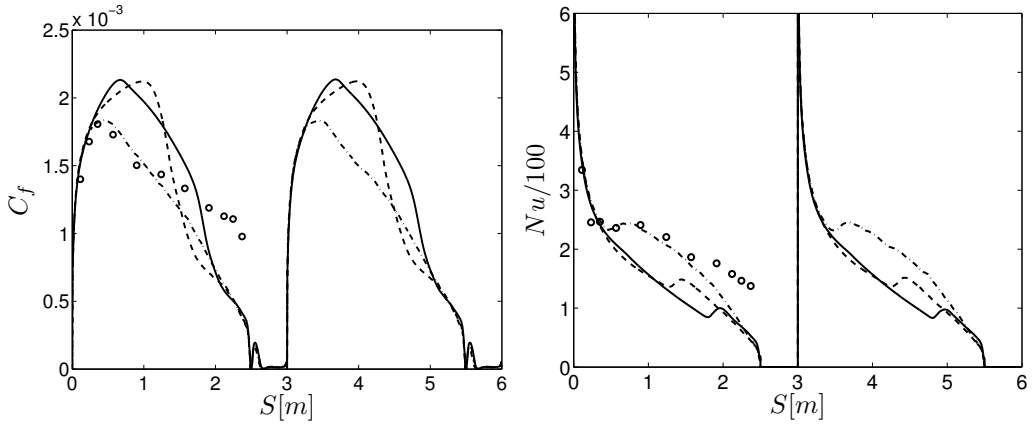

(a) Friction coefficient, C_f

(b) Nusselt number, Nu

Figure 4.19: Friction coefficient and Nusselt number variations along the cavity perimeter. S is the clockwise distance from the lower left corner of the cavity.—— : SMG model; - - - : DYN model; - - - : DNS; ◦ : experiment (King, 1989).

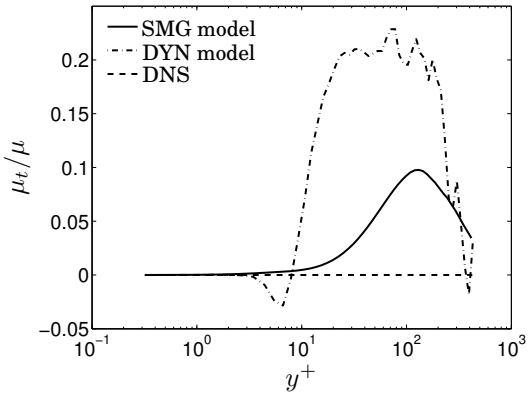

Figure 4.20: Sub-grid scale viscosity variations at $x/L = 0.9$, $Gr = 4.7 \times 10^{10}$.

In the absence of the *SGS* model, one may expect that the transition should have occurred earlier compared to the results of *DYN* model. The reason for the reversed situation is probably the backscatter phenomenon that is appropriately detected by the *DYN* model. This is shown by the negative values of turbulent viscosity in Figure 4.20.

4.3.2 Turbulence parameters

Figure 4.21 compares the computed Reynolds stresses and turbulent heat fluxes with the measurements. The stream-wise Reynolds stress is in good agreement with the experimental results. However, the turbulent shear stress is under-predicted and the stream-wise turbulent heat flux is over-predicted. Similar to the results of the vertical cylinder configuration, there exist a region close to the wall in which the turbulence production due to the turbulent shear stress is positive. Nevertheless both measurements and computations yield a negative turbulent shear stress close to the wall.

4.4 Mixed Convection Boundary Layer in Finite Vertical Channel

The substantial difference between this test case and the other ones is that in the other cases the natural convection boundary layer was the

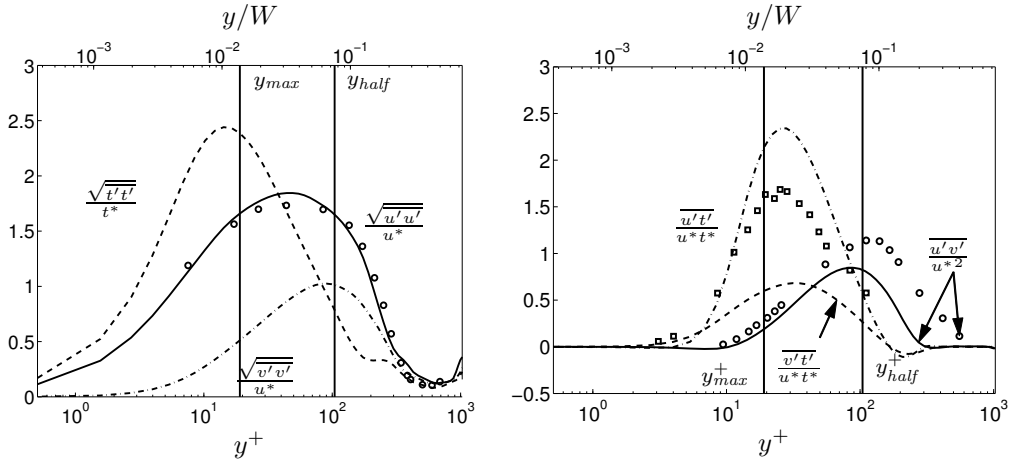

(a) Experimental data from Cheesewright *et al.* (1986).

(b) Experimental data from King (1989).

Figure 4.21: Reynolds stresses and temperature fluctuations at $x/L = 0.5$, $Gr = 8.6 \times 10^9$ for the DYN model and the fine mesh. Lines: simulation, markers: experiments.

subject of the study whereas in this case the boundary layer is of mixed convection type.

The effect of the buoyancy on a mixed convection boundary layer in an infinite channel has already been studied by Davidson *et al.* (2003). However, the existence of the radiation heat transfer and the developing nature of the boundary layer in this configuration made this case unique.

At the inlet the *DNS* results of a fully developed infinite channel were prescribed. Using this boundary condition it was found that the wiggle detector had nearly destroyed the turbulence at the inlet. This can be seen in Figure 4.22.

In Figure 4.22(a), the value zero is the pure *VL* scheme and unity is the pure *CDDC* scheme. The effect of the wiggle detector is largest at the inlet. Farther downstream the wiggle detector is not active (i.e. $\langle \alpha' \rangle$ is close to one which means that the *CDDC* scheme is used) and as a result the turbulent shear stress is preserved.

Initially it was believed that the differences between the experimental results and the simulations were due to the wiggle detector damping the turbulence near the inlet. Therefore in the next step, the wiggle detector was applied only to the temperature and pure *CDDC* scheme

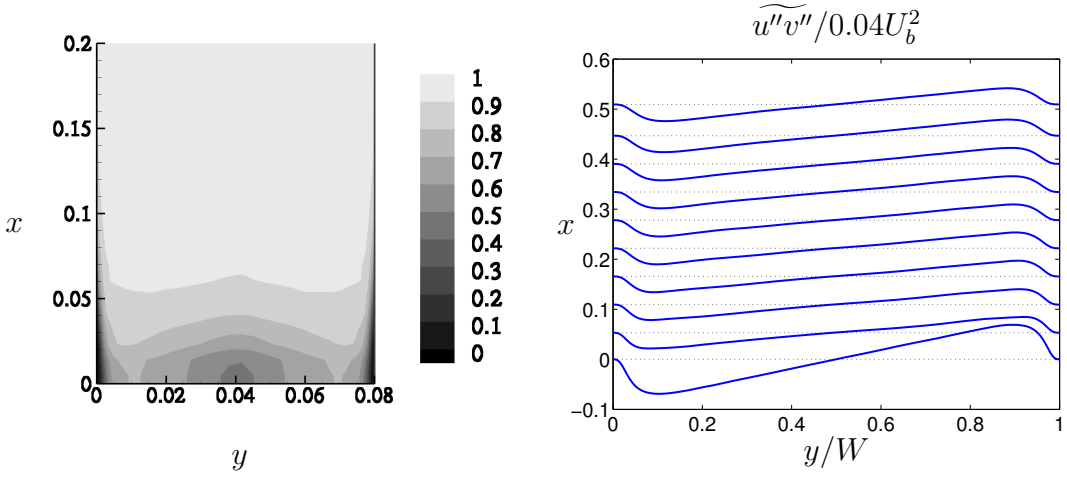

(a) Contours of $\langle \alpha' \rangle$

(b) Turbulent shear stress variations

Figure 4.22: The effect of the wiggle detector on the turbulent shear stress near the inlet.

was used for all velocities. It can be seen from Figure 4.23 that the turbulent shear stress is almost perfectly preserved in the entrance region of the channel by using the pure *CDDC* scheme.

4.4.1 Mean flow parameters

Figure 4.24(a) shows the velocity profiles at $x = 2.5m$ ($x = 3m$ in the case of the measurements) and the Nusselt number variation along the heated channel wall is compared with the measurements in Figure

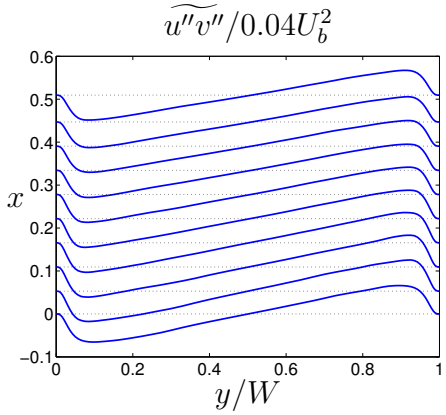

Figure 4.23: The turbulent shear stress at the entrance of the channel using pure *CDDC* scheme.

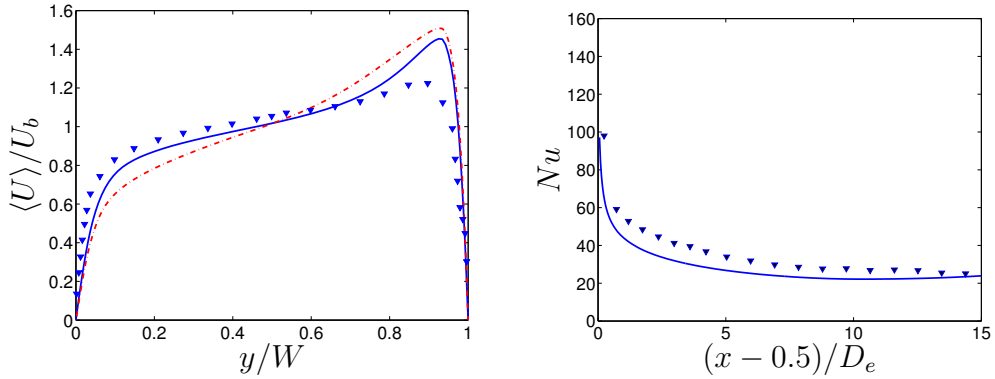

(a) Velocity profile. —— : with radiation; -·-· : neglecting radiation; ▽ : measurements

(b) Nusselt number. —— : Computations; ▽ : measurements. $D_e = 2 \cdot W$

Figure 4.24: Velocity profile and Nusselt number variation.

4.24(b).

It can be seen from Figure 4.24(a) that the radiation heat transfer has a substantial effect on the velocity profile and consequently on the flow regime. Unfortunately, even the acquired mean flow parameters with the pure *CDDC* scheme are not in good agreement with the experimental results.

4.4.2 Turbulence parameters

Employing the pure *CDDC* scheme shows no improvement in the results of the Reynolds shear stresses and turbulent heat fluxes. The discrepancies between the measurements and the simulations remain still high as can be seen in Figure 4.25.

In another attempt, by studying the measured results and computed ones, it was found that the measured results are very similar to the computed results at lower heights of the channel. Therefore it was believed that the reason for these differences could be due to the fact that in the experimental case, the turbulent intensity at the inlet has been much lower than in the simulations and consequently the boundary layer has been developed much slower compared to the computations. Based on this hypothesis, a uniform inlet velocity profile was prescribed at the inlet but it turned out that the level of the turbulence

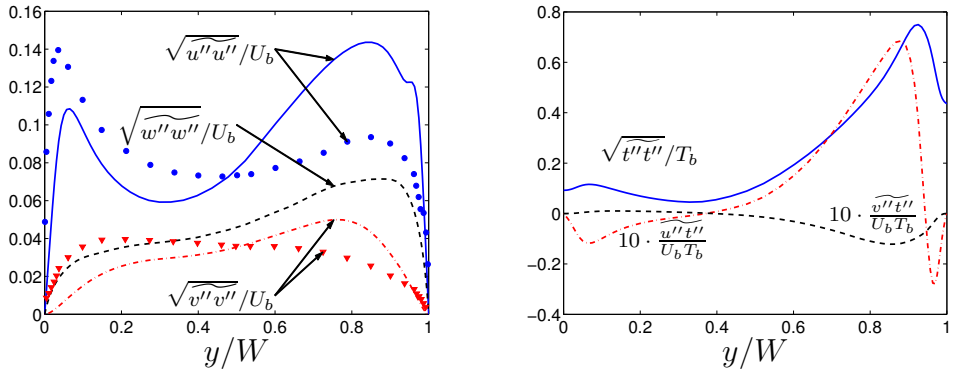

(a) Normal fluctuations.

(b) Turbulent heat fluxes and temperature fluctuations.

Figure 4.25: Reynolds stresses, turbulent heat fluxes and temperature fluctuations in vertical finite channel at $x = 2.5\ m$.

remained very low in the channel and very small values for turbulence parameters obtained. This problem can be studied further, by prescribing artificial velocity profiles with different turbulence intensities at the inlet since the effect of the turbulence at the inlet seems to be decisive for this problem and unfortunately no information are provided from the experiments.

Chapter 5

Concluding Remarks

In the present work, natural convection boundary layers are studied in different geometries. These geometries include a vertical cylinder, a vertical infinite channel and a cavity with the aspect ratio of 5. Besides, a mixed convection boundary layer in a vertical channel is also studied.

In all the cases, *LES* approach is used to simulate the boundary layers. In the case of the finite vertical channel with the mixed convection boundary layer, owing to the high temperature of the channel walls, radiation heat transfer is also taken into account. It is shown that the amount of the radiation heat transfer reaches to as high as 10% of the total wall heat flux and therefore can not be neglected.

The results of the vertical cylinder configuration are compared with the experimental results of Tsuji & Nagano (1988*a*) and Tsuji & Nagano (1988*b*) which are obtained from a vertical flat plate configuration and the experimental results of Persson & Karlsson (1996) which are obtained from a vertical cylinder configuration. It is shown that the predicted results are generally in quantitative agreement with the experimental results. Both the experimental and numerical results of the vertical cylinder configurations show that there exists a region close to the wall (in the inner part of the boundary layer) in which the turbulent shear stress is negative and consequently the shear production is positive. On the contrary, in the case of the vertical flat plate, the experimental results show that the turbulent shear stress remains positive across the boundary layer. The behaviour of the shear stress near the wall affects the production of the stream-wise normal stress. Nevertheless, the predicted locations of the maximum Reynolds stresses and maximum temperature fluctuations match those of the measurements.

The location of the maximum temperature fluctuations lies in the inner part of the boundary layer close to the maximum velocity whereas it lies in the outer part of the boundary layer in the case of the normal and shear stresses.

In the case of the cavity configuration, different *SGS* viscosities are used and it is shown that the dynamic model of Germano *et al.* (1991) is the only model which is capable of predicting the location of the transition region correctly. Results of the calculated turbulent viscosity by this model show that this model has predicted the backscattered energy by associating negative *SGS* viscosity to the flow in some regions. Similar to the case of the vertical cylinder, a region with negative turbulent shear stress exists in the vicinity of the wall. Similar to the cases of the vertical cylinder and vertical flat plate, the stream-wise turbulent heat flux in this case is also negative close to the wall.

In another study, the fully developed natural convection boundary layer in an infinite vertical channel is studied. This geometry configuration yields one-dimensional results. The main objective of this study is to find out whether or not the length of the computational domain has a large influence on the accuracy of the results. It is shown that all the tested computational domains in this study yield almost the same results and therefore, it is possible to acquire domain independent results in this case.

The infinite vertical channel configuration is the only numerical case for which the turbulent shear stress remains positive across the boundary layer. This is similar to the case of the vertical flat plate but contrary to this case, the stream-wise turbulent heat flux in the case of the infinite vertical channel remains also positive near the wall. All the Reynolds stresses and wall-normal turbulent heat flux acquire their maximum at the middle of the channel where the shear stress is large. However, the maximum temperature fluctuations and stream-wise heat flux occur close to the location of the maximum velocity.

Finally, the mixed convection boundary layer in a vertical channel is studied. The high temperature difference between the channel walls and the fluid makes it an appropriate case to study the accuracy of the Boussinesq approximation. Therefore, this case is studied both by assuming Boussinesq approximation and using temperature dependent properties. No substantial differences between the two approaches are observed. Unfortunately, the numerical results deviate from the experimental results substantially. In this case, the instantaneous *DNS* results of a channel flow are prescribed at the inlet but it is shown

that the inlet condition has very little influence (almost negligible) on the results. Thus, it is believed that the reason for the discrepancies between the numerical and experimental results is the uncertainty in the magnitude of the exact wall heat flux in the case of the experiment.

Chapter 6

Future Works

Study of the natural convection boundary layer on the vertical cylinder configuration shows that the results are highly dependent on the angular extent of the computational domain. Although efforts have been made to find the required angle for which the results are independent of the geometry, it will be a valuable experience to confirm the independency of the results from the computational domain by simulating this case in a full cylindrical domain. At the time of this study, such computations were unfeasible since they demand computers with high computational power. An alternative is to develop faster numerical procedures to tackle this kind of flows.

Provided that the fast computers are available, a grid study can be carried out in the case of the cavity configuration to find out what grid resolutions are appropriate for *DNS* computations to yield the accurate results. It is believed that the natural convection boundary layers need higher mesh resolutions compared to the forced convection boundary layers.

Finally, it is recommended to perform simulations of the mixed convection boundary layer in the vertical channel prescribing different boundary conditions at the inlet and channel wall. These conditions should mimic the real experimental conditions as much as possible since it is only in such conditions that the comparison between the experimental and numerical results make sense.

Bibliography

ABE, K., KONDOH, T. & NAGANO, Y. 1994 A new turbulence model for predicting fluid flow and heat transfer in separating and reattaching flows - 1. Flow field calculations. *Int. J. Heat Mass Transfer* **37**, 139–151.

BARHAGHI, D. G., DAVIDSON, L. & KARLSSON, R. 2003 Natural convection heat transfer in a vertical shell and tube. Report 03/01. Dept. of Thermo and Fluid Dynamics, Chalmers University of Technology, Göteborg, Sweden.

BETTS, P. L. & BOKHARI, I. H. 2000 Experiments on turbulent natural convection in an enclosed tall cavity. *International Journal of Heat and Fluid Flow* **21** (6), 675–683.

BURMEISTER, L. C. 1993 *Convective Heat Transfer*. New York: John Wiley & Sons.

CHEESEWRIGHT, R. 1968 Turbulent natural convection from a plane vertical surface. *Journal of Heat Transfer* **90**, 1–8.

CHEESEWRIGHT, R. & IEROKIPIOTIS, E. 1984 Measurements in a turbulent natural convection boundary layer. In *1st UK National Conference on Heat Transfer*, pp. 849–856.

CHEESEWRIGHT, R., KING, K. J. & ZIAI, S. 1986 Experimental data for the validation of computer codes for the prediction of two-dimensional buoyant cavity flows. *ASME Winter Annual Meeting, HTD-60* pp. 75–81.

CUI, A. & STREET, R. L. 2001 Large-eddy simulation of turbulent rotating convective flow development. *J. Fluid Mech.* **447**, 53–84.

DAHLSTRÖM, S. & DAVIDSON, L. 2003 Large eddy simulation applied to a high-reynolds flow around an airfoil close to stall. 41st Aerospace Sciences Meeting, AIAA 2003-0776, Reno.

DAVIDSON, L., ČUTURIĆ, D. & PENG, S.-H. 2003 DNS in a plane vertical channel with and without buoyancy. In *Turbulence Heat and Mass Transfer 4* (ed. K. Hanjalić, Y. Nagano & M. Tummers), pp. 401–408. New York, Wallingford (UK): Begell house, inc.

DAVIDSON, L. & FARHANIEH, B. 1995 CALC-BFC: A finite-volume code employing collocated variable arrangement and cartesian velocity components for computation of fluid flow and heat transfer in complex three-dimensional geometries. Rept. 95/11. Dept. of Thermo and Fluid Dynamics, Chalmers University of Technology, Gothenburg.

DAVIDSON, L. & PENG, S.-H. 2003 Hybrid LES-RANS: A one-equation SGS model combined with a $k - \omega$ model for predicting recirculating flows. *International Journal for Numerical Methods in Fluids* **43**, 1003–1018.

VAN DRIEST, E. R. 1956 On turbulent flow near a wall. *J. Aero. Sci.* **23**, 1007–1011.

EIDSON, T. M. 1985 Numerical simulation of the turbulent Rayleigh-Bénard problem using subgrid modelling. *Journal of Fluid Mechanics* **158**, 245–268.

EMVIN, P. 1997 The full multigrid method applied to turbulent flow in ventilated enclosures using structured and unstructured grids. PhD thesis, Dept. of Thermo and Fluid Dynamics, Chalmers University of Technology, Göteborg.

FERZIGER, J. H. & PERIC, M. 1996 *Computational Methods for Fluid Dynamics*. Berlin: Springer-Verlag.

FUJII, T., TAKEUCHI, M., FUJII, M., SUZAKI, K. & UEHARA, H. 1970 Experiments on natural-convection heat transfer from the outer surface of a vertical cylinder to liquids. *Int. J. Heat Mass Transfer* **13**, 753–787.

GEORGE, W. K. & CAPP, S. P. 1979 A theory for natural convection turbulent boundary layers next to heated vertical surfaces. *International Journal of Heat and Mass Transfer* **22**, 813–826.

GERMANO, M., PIOMELLI, U., MOIN, P. & CABOT, W. H. 1991 A dynamic subgrid-scale eddy viscosity model. *Physics of Fluids A* **3**, 1760–1765.

GOLDSTEIN, R. J., ECKERT, E. R. G., IBELE, W. E., PATANKAR, S. V., SIMON, T. W., KUEHN, T. H., STRYKOWSKI, P. J., TAMMA, K. K., BAR-COHEN, A., HEBERLEIN, J. V. R., DAVIDSON, J. H., BISCHOF, J., KULACKI, F. A., KORTSHAGEN, U. & GARRICK, S. 2002 Heat transfer - a review of 2000 literature. *International Journal of Heat and Mass Transfer* **45** (14), 2853–2957.

KALTENBACH, H. J., FATICA, M., MITTAL, R., LUND, T. S. & MOIN, P. 1999 Study of flow in a planar asymmetric diffuser using large-eddy simulation. *Journal of Fluid Mechanics* **390**, 151–185.

KING, K. J. 1989 Turbulent natural convection in rectangular air cavities. PhD thesis, Queen Mary College, University of London, London, UK.

KITAMURA, K., KOIKE, M., FUKUOKA, I. & SAITO, T. 1985 Large eddy structure and heat transfer of turbulent natural convection along a vertical flat plate. *Int. J. Heat Mass Transfer* **28**, 837–850.

KOTSOVINOS, N. E. 1991 Turbulence spectra in free convection flow. *Physics of Fluids A* **3** (1), 163–167.

KUTATELADZE, S. S., KIRDYASHKIN, A. G. & IVAKIN, V. P. 1972 Turbulent natural convection on a vertical plate and in a vertical layer. *Int. J. Heat Mass Transfer* **15**, 193–202.

LILLY, D. K. 1992 A proposed modification of the Germano subgrid-scale closure method. *Physics of Fluids A* **4**, 633–635.

LOCK, G. S. H. & TROTTER, F. J. D. 1968 Observations on the structure of a turbulent free convection boundary layer. *Int. J. Heat Mass Transfer* **11**, 1225–1232.

MARY, I. & SAGAUT, P. 2002 Large eddy simulation of flow around an airfoil near stall. *AIAA Journal* **40** (6), 1139–1145.

MIKI, Y., FUKUDA, K. & TANIGUCHI, N. 1993 Large eddy simulation of turbulent natural convection in concentric horizontal annuli. *Int. J. Heat and Fluid Flow* **14**, 210–216.

MIYAMOTO, M., KAJINO, H., KURIMA, J. & TAKANAMI, I. 1982 Development of turbulence characteristics in a vertical free convection boundary layer. In *7th Int. Heat Transfer Conference*, pp. 323–328. Munich.

MURAKAMI, S. 1997 Current status and future trends in computational wind engineering. *Journal of Wind Engineering and Industrial Aerodynamics* **67**, 3–34.

NICOUD, F. & DUCROS, F. 1999 Subgrid-scale stress modelling based on the square of the velocity gradient tensor. *Flow, Turbulence and Combustion* **62**, 183–200.

NIEUWSTADT, F. T. M. & VERSTEEGH, T. A. M. 1997 DNS of natural convection between two vertical,differentially heated walls. In *Proc. 11th Symp. on Turbulent Shear Flows*. Grenoble.

NINGYU, L., XIYUN, L. & LIXIAN, Z. 2000 A dynamic subgrid-scale model for the large eddy simulation of stratified flow. *Science in China* **43** (4), 391–399.

OSTRACH, S. 1952 An analysis of laminar free-convection flow and heat transfer about a plate parallel to the direction of the generating body force. Report 1111. NACA.

PAOLUCCI, S. 1990 Direct numerical simulation of two-dimensional turbulent natural convection in an enclosed cavity. *Journal of Fluid Mechanics* **215**, 229–262.

PAOLUCCI, S. & CHENOWETH, D. R. 1987 Transition to chaos in a differentially heated vertical cavity. *Journal of Fluid Mechanics* **201**, 379–410.

PENG, S.-H. & DAVIDSON, L. 1998 Comparison of subgrid-scale models in LES for turbulent convection flow with heat transfer. In *2nd EF Conference in Turbulent Heat Transfer*, , vol. 1, pp. 5.24–5.35. Manchester.

PENG, S.-H. & DAVIDSON, L. 2001*a* Comparative study of LES for turbulent buoyant flow in terms of SGS model and grid resolution. In *The Second International Symp. on Turbulence and Shear Flow Phenomena* (ed. E. Lindborg, A. Johansson, J. Eaton, J. Humphrey, N. Kasagi, M. Leschziner & M. Sommerfeld), , vol. 2, pp. 455–460. Stockholm.

PENG, S.-H. & DAVIDSON, L. 2001*b* Large eddy simulation for turbulent buoyant flow in a confined cavity. *International Journal of Heat and Fluid Flow* **22**, 323–331.

PENG, S.-H. & DAVIDSON, L. 2002 On a subgrid-scale heat flux model for large eddy simulation of turbulent thermal flow. *International Journal of Heat and Mass Transfer* **45**, 1393–1405.

PENG, S.-H., DAVIDSON, L. & HOLMBERG, S. 1997 A modified low-Reynolds-number $k-\omega$ model for recirculating flows. *ASME: Journal of Fluids Engineering* **119**, 867–875.

PERSSON, N. J. & KARLSSON, R. I. 1996 Turbulent natural convection around a heated vertical slender cylinder. In *8th Int. Symp. on Applications of Laser Techniques to Fluid Mechanics*. Lisbon.

POPE, S. B. 2000 *Turbulent Flows*. Cambridge, United Kingdom: Cambridge University Press.

SMAGORINSKY, J. 1963 General circulation experiments with the primitive equations. *Monthly Weather Review* **91**, 99–165.

SOHANKAR, A., NORBERG, C. & DAVIDSON, L. 1998 Low-Reynolds number flow around a square cylinder at incidence: Study of blockage, onset of vortex shedding and outlet boundary condition. *International Journal for Numerical Methods in Fluids* **26**, 39–56.

SORIA, M., TRIAS, F. X., PÉREZ-SEGARRA, C. D. & OLIVA, A. 2004 Direct numerical simulation of a three-dimensional natural-convection flow in a differentially heated cavity of aspect ratio 4. *Numerical Heat Transfer. Part A* **45** (7), 649 – 673.

TIAN, Y. S. & KARAYIANNIS, T. G. 2000*a* Low turbulence natural convection in an air filled square cavity part i: the thermal and fluid flow fields. *International Journal of Heat and Mass Transfer* **43**, 849–866.

TIAN, Y. S. & KARAYIANNIS, T. G. 2000*b* Low turbulence natural convection in an air filled square cavity part ii: the turbulence quantities. *International Journal of Heat and Mass Transfer* **43**, 867–884.

TSUJI, T. & NAGANO, Y. 1988*a* Characteristics of a turbulent natural convection boundary layer along a vertical flat plate. *International Journal of Heat and Mass Transfer* **31** (8), 1723–1734.

TSUJI, T. & NAGANO, Y. 1988*b* Turbulence measurements in a natural convection boundary layer along a vertical flat plate. *International Journal of Heat and Mass Transfer* **31** (10), 2101–2111.

VERSTEEGH, H. K. & MALALASEKERA, W. 1995 *An Introduction to Computational Fluid Dynamics - The Finite Volume Method*. Harlow, England: Longman Scientific & Technical.

VERSTEEGH, T. A. M. & NIEUWSTADT, F. T. M. 1998 Turbulent budgets of natural convection in an infinite, differentially heated, vertical channel. *International Journal of Heat and Fluid Flow* **19**, 135–149.

VLIET, G. C. & LIU, C. K. 1969 An experimental study of turbulent natural convection boundary layers. *Journal of Heat Transfer* **91**, 517–531.

WANG, J., LI, J. & JACKSON, J. D. 2004 A study of the influence of buoyancy on turbulent flow in a vertical plane passage. *International Journal of Heat and Fluid Flow* **25** (3), 420–430.

WARNER, C. Y. & ARPACI, V. S. 1968 An experimental investigation of turbulent natural convection in air at low pressure along a vertival heated flat plate. *Int. J. Heat Mass Transfer* **11**, 397–406.

WOSNIK, M. & GEORGE, W. K. 1995 Another look at the turbulent natural convection boundary layer next to heated vertical surfaces. In *ICHMT Symposium on Turbulence, Heat and Mass Transfer*. Lisbon.

ZHANG, W. & CHEN, Q. 2000 Large eddy simulation of indoor airflow with a filtered dynamic subgrid scale model. *International Journal of Heat and Mass Transfer* **43**, 3219–3231.

Appendix A

Effect of Sample Size on Ensemble Averaging

The number of samples in calculating statistical parameters is an important issue. However, it is not quite clear how many samples are essential to yield the required accuracy.

To study the effect of sample size on the accuracy of the turbulent parameters, approximately $290,000$ samples of the stream-wise velocity at each time step are extracted from LES computations of the $5:1$ cavity at four different points. All these points lie in the mid-height of the cavity at distances $y^+ \approx 4$, 12, 45 and 190 from the wall.

The autocorrelation curves at these points and the corresponding integral time scales (T_{int}) are shown in Figure A.1. In the computations the time step is equal to $\Delta t = 6.25 \times 10^{-3} sec$. Based on this, the number of acquired independent (uncorrelated samples in which case the time interval between two contiguous samples is larger than the integral time scale) samples NIS are also computed at each point. It can be seen that the time scale increases as the distance from the wall increases or in other words the turbulent structures are getting bigger farther away from the wall.

In Table A.1 the mean velocity and turbulent parameters are compared using independent (uncorrelated) and all samples. In the experiments, statistical parameters are usually calculated using independent (uncorrelated) samples whereas in the *CFD* computations samples are usually correlated. It can be seen that at higher moments the difference between the two approaches increases.

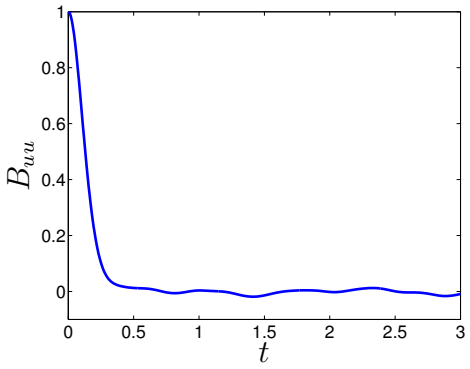

(a) At $y^+ \approx 4$, $T_{int} = 0.29sec$ and $NIS = 6250$.

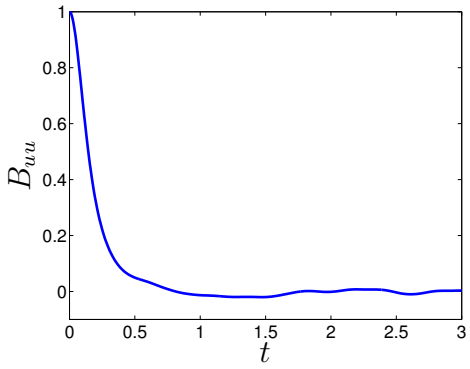

(b) At $y^+ \approx 12$, $T_{int} = 0.37sec$ and $NIS = 4900$.

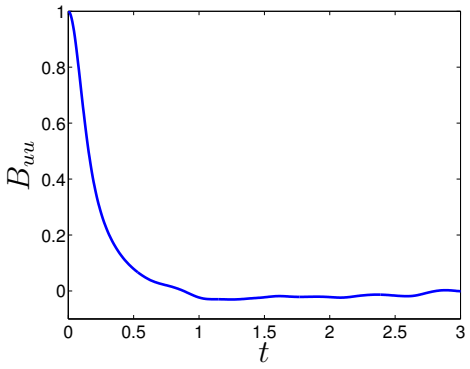

(c) At $y^+ \approx 45$, $T_{int} = 0.42sec$ and $NIS = 4300$.

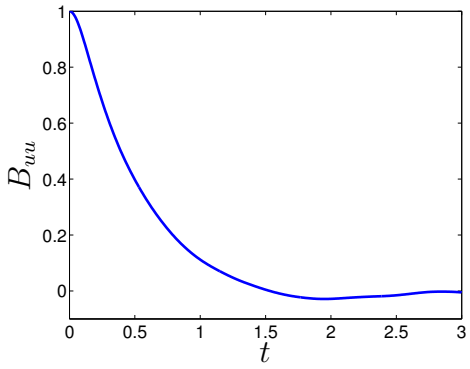

(d) At $y^+ \approx 190$, $T_{int} = 0.98sec$ and $NIS = 1850$.

Figure A.1: Autocorrelation curves of the stream-wise velocity at different distances from the wall.

	Based on all samples	Based on independent samples	Difference
$\langle u \rangle$	0.1605	0.1604	0.1%
$\langle u'u' \rangle$	0.00147	0.00143	2.9%
$\langle u'u'u' \rangle$	0.000022	0.000019	13%

Table A.1: Calculation of the mean velocity and turbulent parameters at $y^+ \approx 4$ using all samples and independent samples.

To study the effect of the sample size, the first (mean) and second moments of the stream-wise velocity are calculated using different number of samples. The lowest number of samples which is used is $N = 15000$ and the highest number of samples is $N = 90000$. The statistical parameters are calculated 200 times for each sample size, N, and at each time the starting point is chosen randomly. The results are shown in Figure A.2. The horizontal lines are the calculated moments when all samples are used.

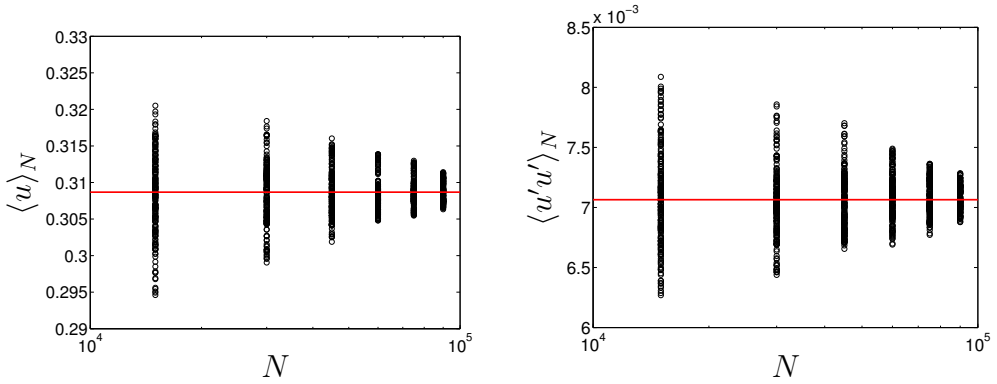

(a) The first moment (mean) of u.

(b) The second moment (variance) of u.

Figure A.2: The effect of the sample size on the calculation of the first and second moment of the stream-wise velocity at $y^+ = 12$.

It can be seen that the calculated parameters are approaching to the targeted value as the sample size increases. This can be better seen by defining the *RMS* scatter of the mean and the second moments as follows:

$$\overline{u}_{sct} = \left\{ \frac{1}{200} \sum_{i=1}^{200} \left[\left(\langle u \rangle_N \right)_i - \langle u \rangle \right]^2 \right\}^{1/2} \tag{A.1}$$

$$\overline{u'u'}_{sct} = \left\{ \frac{1}{200} \sum_{i=1}^{200} \left[\left(\langle u'u' \rangle_N \right)_i - \langle u'u' \rangle \right]^2 \right\}^{1/2} \tag{A.2}$$

The variation of $\overline{u}_{sct}$ and $\overline{u'u'}_{sct}$ at different locations, for different sample sizes are shown in Figure A.3. I is the local turbulence intensity. The linear variation of these plots suggests that the *RMS* scatter of the first and second moments are a logarithmic function of the sample size.

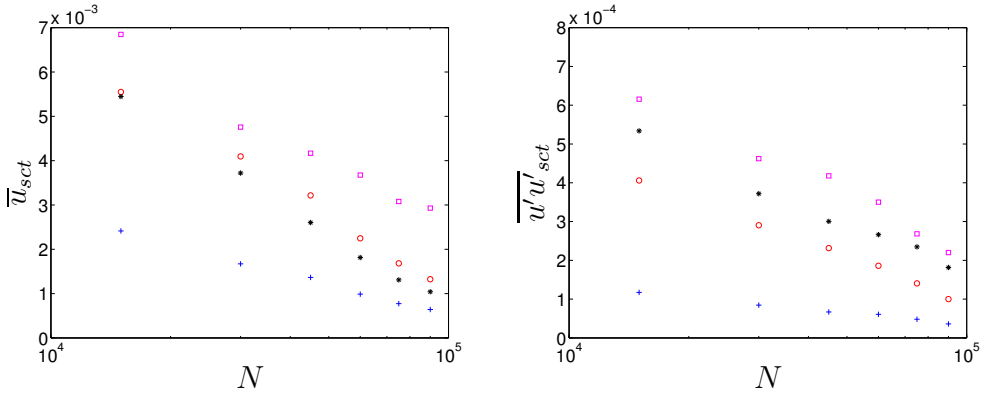

(a) *RMS* scatter of the first moment.

(b) *RMS* scatter of the second moment.

Figure A.3: Variation of the *RMS* scatter of the first and second moments for different number of samples. + : $y^+ = 4$, $I = 23\%$; ∘ : $y^+ = 12$, $I = 27\%$; ∗ : $y^+ = 45$, $I = 35\%$; □ : $y^+ = 190$, $I = 83\%$.

The theoretical estimated error of the first and second moments of a variable x read:

$$\epsilon^2_{X_N} = \frac{1}{N}\frac{\langle (x-X)^2 \rangle}{X^2} \tag{A.3}$$

$$\epsilon^2_{\langle (x-X)^2 \rangle_N} = \frac{1}{N}\left[\frac{\langle (x-X)^4 \rangle}{\langle (x-X)^2 \rangle^2} - 1\right] \tag{A.4}$$

in which X_N is the mean or first moment based on N independent samples and X is the true mean value (based on all samples). The theoretical error is calculated and shown in Figure A.4. The computed error in Figure A.4(a) is somewhat larger than the theoretical one for smaller sample sizes. However this error becomes smaller for larger number of samples. On the other hand the computed error of the second moment never exceeds the corresponding theoretical one.

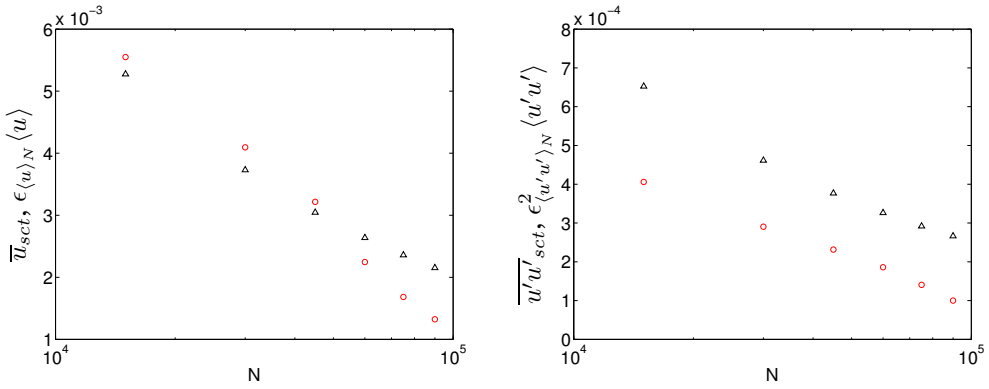

(a) The first moment (mean) error.

(b) The second moment (variance) error.

Figure A.4: Comparison of the theoretical mean error and the computed one for the first and second moments at $y^+ = 12$. $\circ$: Computed error; $\triangledown$: theoretical error.

Appendix B

Energy Spectrum Calculation

Assume that $f(x)$, $-\infty < x < \infty$, is piece-wise differentiable and absolutely integrable. The Fourier transform of the function $f(x)$ is defined as:

$$F(k) = \hat{f}(k) = \frac{1}{2\pi} \int_{-\infty}^{\infty} f(x) e^{-ikx} dx \tag{B.1}$$

Suppose that $\{f(x_n)\}_{n=1..N}$ is a set of N-periodic complex-valued data for which:

$$f(x_1) = f(x_{N+1})$$

The discrete Fourier transform or DFT of this set of data is defined as:

$$F(k_m) = \hat{f}(k_m) = \sum_{n=1}^{N} f(x_n) e^{-2\pi i(m-1)(n-1)/N}, \qquad \text{for } m = 1..N \tag{B.2}$$

To calculate the discrete Fourier transform of a set of data, many mathematical operations are needed. Hence, the computation of a large set of data can be very time consuming. Fast Fourier transform or FFT is an algorithm which reduces the number of operations for DFT if $N = 2^i$ in which i is a natural number. The FFT algorithm is a built-in function

in most of the mathematical packages such as MATLAB™. However, these packages design the FFT functions in a general way in order to be useful in all kind of applications. For the purpose of energy spectrum, the FFT in MATLAB™should be modified. Considering Equation B.1, the FFT estimation of it is computed as follows:

$$\begin{aligned}
\hat{f}(k) &= \frac{1}{2\pi}\int_{-\infty}^{\infty} f(x)e^{-ikx}dx \\
\hat{f}(k_m) &= \frac{1}{2\pi}\sum_{n=1}^{N} f(x_n)e^{-i[\frac{2\pi}{L}(m-1)][(n-1)\Delta x]}\Delta x \\
&= \frac{1}{2\pi}\Delta x\sum_{n=1}^{N} f(x_n)e^{-i[\frac{2\pi}{L}(m-1)][(n-1)\frac{L}{N}]} \\
&= \frac{\Delta x}{2\pi}\sum_{n=1}^{N} f(x_n)e^{-2\pi i(m-1)(n-1)/N} \\
&= \frac{\Delta x}{2\pi}FFT(f(x_n)),\ \ m = 1..N,\ \ k_m = \frac{2\pi}{L}(m-1)
\end{aligned}$$

In the present work, as the cyclic boundary condition is the θ direction, the energy spectra of the spatial two-point correlations at radius R are calculated as follows (Note that the energy spectrum is defined as the *twice* of the Fourier transform of the two-point correlation function):

$$\begin{aligned}
E_{ij}(\kappa_m) &= 2\cdot\frac{R\Delta\theta}{2\pi}\sum_{n=1}^{N} R_{ij}(n)e^{-2\pi i(m-1)(n-1)/N} \\
&= \frac{R\Delta\theta}{\pi}FFT(R_{ij}(n))
\end{aligned} \tag{B.3}$$

In which:

$$\begin{cases}
m = 1..N \\
\kappa_m = 2\pi(m-1)/(R\cdot\theta_{\mathit{eff}}) \\
\Delta\theta = \theta_{max}/(n_k-1) \\
\theta_{\mathit{eff}} = N\Delta\theta
\end{cases}$$

n_k is the number of nodes in the θ-direction. For the present LES results, $n_k = 162$ and $\theta_{max} = \pi/2$. It should be mentioned that in the

present work $N = n_k - 2 = 160$. The reason is that since cyclic boundary condition is applied in the θ-direction, the 1^{st} node is the same as $(n_k - 1)^{th}$ node and the 2^{nd} node is the same as n_k^{th} node. This means that the effective span-wise extension is in fact $(n_k - 2)\Delta\theta$. Also $R_{ij}(n_k - 1) = R_{ij}(1)$ showing that $N + 1 = n_k - 1$ or $N = n_k - 2$. This is shown in Figure B.1.

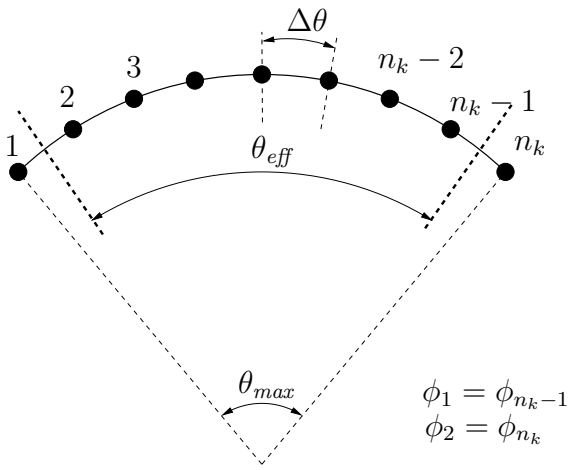

Figure B.1: Schematic diagram of a grid with cyclic boundary conditions in θ direction.

Paper I

Paper II

Paper III

Paper IV

Paper V

Paper VI